JOURNAL OF GEOPHYSICAL RESEARCH, VOL. 106, NO. B1, PAGES 537–552, JANUARY 10, 2001

Flow of variably fluidized granular masses across three-dimensional terrain
1. Coulomb mixture theory

Richard M. Iverson and Roger P. Denlinger
U.S. Geological Survey, Vancouver, Washington

Abstract. Rock avalanches, debris flows, and related phenomena consist of grain-fluid mixtures that move across three-dimensional terrain. In all these phenomena the same basic forces govern motion, but differing mixture compositions, initial conditions, and boundary conditions yield varied dynamics and deposits. To predict motion of diverse grain-fluid masses from initiation to deposition, we develop a depth-averaged, three-dimensional mathematical model that accounts explicitly for solid- and fluid-phase forces and interactions. Model input consists of initial conditions, path topography, basal and internal friction angles of solid grains, viscosity of pore fluid, mixture density, and a mixture diffusivity that controls pore pressure dissipation. Because these properties are constrained by independent measurements, the model requires little or no calibration and yields readily testable predictions. In the limit of vanishing Coulomb friction due to persistent high fluid pressure the model equations describe motion of viscous floods, and in the limit of vanishing fluid stress they describe one-phase granular avalanches. Analysis of intermediate phenomena such as debris flows and pyroclastic flows requires use of the full mixture equations, which can simulate interaction of high-friction surge fronts with more-fluid debris that follows. Special numerical methods (described in the companion paper) are necessary to solve the full equations, but exact analytical solutions of simplified equations provide critical insight. An analytical solution for translational motion of a Coulomb mixture accelerating from rest and descending a uniform slope demonstrates that steady flow can occur only asymptotically. A solution for the asymptotic limit of steady flow in a rectangular channel explains why shear may be concentrated in narrow marginal bands that border a plug of translating debris. Solutions for static equilibrium of source areas describe conditions of incipient slope instability, and other static solutions show that nonuniform distributions of pore fluid pressure produce bluntly tapered vertical profiles at the margins of deposits. Simplified equations and solutions may apply in additional situations identified by a scaling analysis. Assessment of dimensionless scaling parameters also reveals that miniature laboratory experiments poorly simulate the dynamics of full-scale flows in which fluid effects are significant. Therefore large geophysical flows can exhibit dynamics not evident at laboratory scales.

1. Introduction

Gravity-driven flows of dense grain-fluid mixtures with free upper surfaces occur commonly on the Earth's surface, sometimes with devastating consequences. Examples range from dry rock avalanches, in which pore fluid may play a negligible role, to liquid-saturated debris flows and gas-charged pyroclastic flows, in which fluids may enhance bulk mobility. Many investigators have modeled these events mathematically by specifying rheological rules that govern flow behavior. In general, however, specified rheologies are neither well-constrained nor sufficient to explain flow dynamics, because steady, uniform, rheometric flows of grain-fluid mixtures do not occur in nature.

Here we investigate a simpler hypothesis, which holds that most gravity-driven, grain-fluid flows obey no particular stress–strain rate relation. Instead, intergranular stresses satisfy the familiar Coulomb rule, and variations in flow behavior result mostly from the varying effects of pore fluid, topography, and inertial forces. To date, however, a Coulomb model applicable to geophysical flows across three-dimensional terrain has been lacking because conceptual and computational problems have thwarted efforts to combine the influences of Coulomb friction, pore fluid stresses, bed topography, and flow inertia in a satisfactory manner. We solve these problems to develop a Coulomb mixture model applicable to diverse geophysical flows, from dry granular avalanches to liquefied slurry floods. Use of a single model to describe a spectrum of flows helps clarify the physical basis of similarities and differences among events.

The model we develop is a generalization of the depth-averaged, two-dimensional grain-fluid mixture model of *Iverson* [1997a, 1997b], who in turn generalized the one-phase grain flow model of *Savage and Hutter* [1989, 1991]. Our new generalization yields depth-averaged mass and momentum balance equations that describe finite masses of variably fluidized grain-fluid mixtures that move unsteadily across three-dimensional terrain, from initiation to deposition. In generalizing to three spatial dimensions we address key physical issues

Paper number 2000JB900329.

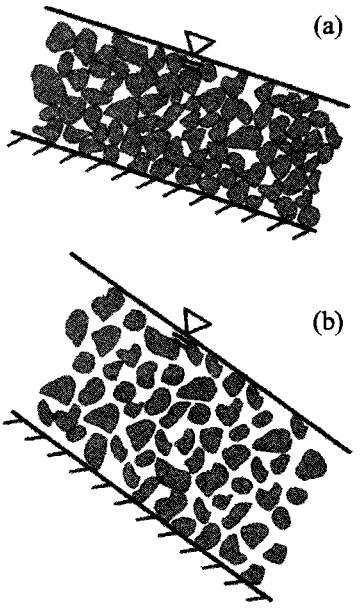

Figure 1. Schematic vertical cross sections of steady, uniform, gravity-driven flows of grain-fluid mixtures down inclined planes. (a) Highly concentrated, friction-dominated flow regime. (b) Highly dilated, collision-dominated flow regime.

concerning preservation of frame invariance, symmetry of conjugate shear stresses, magnitudes of lateral forces, and distributions of pore fluid pressure. The companion paper by *Denlinger and Iverson* [this issue] describes a robust numerical method for solving the equations and tests numerical predictions against experimental data.

2. Coulomb Mixture Behavior

Abundant data confirm the validity of *Coulomb*'s [1776] model of rate-independent frictional deformation in diverse granular materials [*Brown and Richards*, 1970; *Duran*, 2000]. The success of the Coulomb friction model for characterizing continuum-scale stresses in slowly deforming granular materials makes it the most parsimonious "null hypothesis" model of continuum stresses in moderately rapid grain flows as well [*Savage and Hutter*, 1989; *Adams and Briscoe*, 1994]. However, in very rapid granular flows, brief collisions rather than prolonged frictional contacts dominate intergranular momentum transport [*Savage*, 1984]. We discuss the limits of Coulomb frictional behavior, as well as the influence of intergranular fluid, before we describe our mathematical model.

Influences of Coulomb friction and grain collisions on gravity-driven granular flows can be evaluated using a numerical criterion identified by *Savage* [1984], defined more explicitly by *Savage and Hutter* [1989], and generalized by *Iverson* [1997a] to account for the presence of pore fluid at equilibrium pressure. This criterion distinguishes flow regimes on the basis of a dimensionless parameter, N_S, that characterizes stresses in steady, uniform flows (Figure 1),

$$N_S = \frac{\rho_s \dot{\gamma}^2 \delta^2}{(\rho_s - \rho_f) g H}, \tag{1}$$

where ρ_s and ρ_f are the mass densities of the solid grains and intergranular fluid, respectively, $\dot{\gamma}$ is the bulk (continuum) shear strain rate, δ is the grain diameter, g is the magnitude of gravitational acceleration, and H is depth below the flow surface. Roughly, N_S represents the ratio of grain collision stresses to gravitational grain contact stresses that produce Coulomb friction. On the basis of diverse data, *Savage and Hutter* [1989] inferred that if $N_S > 0.1$ at typical depths H, grain collision stresses may affect flow dynamics significantly. Table 1 lists values of N_S and related dimensionless parameters estimated for some well-documented geophysical flows. The tabulated values indicate that many geophysical flows probably fall within the friction-dominated rather than collision-dominated regime.

Intergranular pore fluid pressures influence Coulomb friction in deforming granular masses and may differ from the steady equilibrium pressures assumed in (1). Calculations and data indicate that *Terzaghi*'s [1936] effective stress principle can describe these pore pressure effects even if deformations are large and moderately rapid [*Iverson and LaHusen*, 1989; *Iverson*, 1993]. The Coulomb equation with pore pressure effects can be stated in several forms, including three we use here:

$$\tau_{\text{yield}} = (\sigma_{\text{yield}} - p) \tan \varphi + c, \tag{2a}$$

$$\tau_{\text{maximum}} = (\sigma_{\text{mean}} - p) \sin \varphi + c \cos \varphi, \tag{2b}$$

$$\left[\left(\frac{\sigma_{xx} - \sigma_{yy}}{2} \right)^2 + \tau_{yx}^2 \right]^{1/2} = \left[\left(\frac{\sigma_{xx} + \sigma_{yy}}{2} \right) - p \right] \sin \varphi + c \cos \varphi, \tag{2c}$$

where τ is the intergranular shear stress, σ is the total compressive normal stress, p is the pore fluid pressure, φ is the intergranular Coulomb friction angle, c is the intergranular cohesion, and $\sigma - p$ is the intergranular effective stress. Subscripts denote whether stresses act on yield planes (as in (2a)), on planes of maximum shear stress and mean normal stress (as in (2b)), or on arbitrary planes defined by a rectangular Cartesian coordinate system (as in (2c)). Importantly, these equations indicate that stress components with no resultant in the plane of yielding (for example, stresses acting in the z direction in the case of (2c)) do not influence in-plane yielding, a fundamental feature of Coulomb behavior. More elaborate formulations of the effective stress principle and Coulomb equation are possible [*Passman and McTigue*, 1986; *Desai and Siriwardane*, 1984], but our analysis uses the simple forms (2a), (2b), and (2c).

Shear cell experiments first conducted by *Bagnold* [1954] and subsequently replicated by others reveal that an equation identical to the Coulomb equation with $c = 0$ adequately describes the relationship between bulk intergranular normal and shear stresses even in collision-dominated flows with $N_S \to \infty$. (*Bagnold* [1954] eliminated gravitationally induced Coulomb friction in his experiments by using neutrally buoyant grain-fluid mixtures in which $\rho_s = \rho_f$. Comparable conditions with no Coulomb friction can occur transiently in geophysical flows, but only if high fluid pressures cause complete mixture fluidization or liquefaction, mimicking the condition $\rho_s = \rho_f$.) *Bagnold* [1954] also found that bulk normal stresses in rapid, collision-dominated flows depend on shear rate, whereas this dependence is absent in slower, friction-dominated flows. Bulk normal stresses in rapid ($N_S > 0.1$) gravity-driven flows with free upper surfaces differ from those in slower flows because

Table 1. Typical Values of Physical and Dimensionless Parameters Estimated for Some Well-Documented Grain-Fluid Flows[a]

		Flow Location and Type			
	Symbol (Units)	USGS Flume Debris Flows[b]	Yake Dake Debris Flows[c]	Mount St. Helens Pyroclastic Flows[d]	Elm Rock Avalanche[e]
Physical parameters					
Friction angles	φ_{int}, φ_{bed} (deg)	28–42	25–50	25–50	25–50
Solid volume fraction	v_s (none)	0.6	0.6	0.4	0.5
Fluid volume fraction	v_f (none)	0.4	0.4	0.6	0.5
Solid density	ρ_s (kg/m^3)	2700	2600	2600	2400
Fluid density	ρ_f (kg/m^3)	1200[f]	1200[f]	2[g]	2[g]
Fluid viscosity	μ (Pa-s)	0.1[f]	0.1[f]	2×10^{-5} [g]	2×10^{-5} [g]
Typical grain diameter	δ (m)	0.01	0.2	0.01	0.5
Mixture density	ρ (kg/m^3)	2000	2000	1000	1200
Hydraulic permeability	k (m^2)	10^{-11}	10^{-8}	10^{-11}	10^{-8}
Hydraulic diffusivity	D (m^2/s)	10^{-4}	0.001	0.01	0.1
Flow shear rate	$\dot{\gamma}$ (1/s)	50	3	10	5
Flow thickness	H (m)	0.2	2	1	10
Flow length	L (m)	100	1000	2000	2000
Dimensionless parameters					
Flow aspect ratio	ε	0.002	0.002	0.0005	0.005
Savage number	N_S	0.2	0.03	0.001	0.06
Bagnold number	N_B	600	1×10^4	3×10^5	4×10^8
Quasi-Reynolds number	N_R	3×10^5	1×10^7	1×10^{10}	8×10^{10}
Fluidization number	N_f	7×10^{-8}	2×10^{-5}	6×10^{-5}	0.08
Pore pressure number	N_p	0.008	0.002	0.1	0.06

[a]To estimate Bagnold numbers, maximum volume fractions of solid grains were assumed equal to 0.7.
[b]*Iverson* [1997a].
[c]*Takahashi* [1991].
[d]*Rowley et al.* [1981], *Wilson and Head* [1981], and *Hoblitt* [1986].
[e]*Hsu* [1975, 1978].
[f]Muddy water.
[g]Dusty air.

shear rate–dependent grain collisions reduce the mixture unit weight by dilating the granular phase (Figure 1). Regardless of the shear rate or degree of dilation, however, the Coulomb equation adequately describes bulk intergranular shear stresses that arise in reaction to the slope-parallel component of the mixture weight.

Bagnold's [1954] experiments also assessed the role of viscous fluid stresses in granular mixtures. *Bagnold* [1954] distinguished contributions of grain collision and viscous stresses in steady, uniform shear flows on the basis of a dimensionless parameter, N_B, defined as

$$N_B = \left[\frac{v_s^{1/3}}{v_*^{1/3} - v_s^{1/3}} \right]^{1/2} \frac{\rho_s \dot{\gamma} \delta^2}{\mu}. \quad (3)$$

Values of this parameter depend on the same properties used to calculate N_S and also depend on v_s, the volume fraction (concentration) of the granular solids; v_*, the maximum (close-packed) value of v_s; and μ, the viscosity of the intergranular fluid. Values of N_B smaller than ~40 indicate *Bagnold*'s [1954] "macroviscous" regime, in which bulk normal and shear stresses are both proportional to the shear rate, $\dot{\gamma}$. Values of N_B larger than ~450 indicate a collision-dominated flow regime in which bulk normal and shear stresses are both proportional to $\dot{\gamma}^2$ [*Bagnold*, 1954; *Savage and Sayed*, 1984].

The term in brackets in (3) highlights the important influence of grain concentration v_s on the stress regime. In the dense flow limit ($v_s \to v_*$), the term in brackets approaches ∞, indicating that collisional stresses greatly surpass viscous stresses. However, in dense geophysical flows with free upper surfaces, gH generally exceeds $\dot{\gamma}^2\delta^2$ very significantly; then $N_S < 0.1$, and Coulomb friction due to gravitational stress may surpass all other forms of shear resistance. Most debris flows and rock avalanches appear to have $v_s > 0.5$, not far from the dense flow limit, whereas little is known about grain concentrations in moving pyroclastic flows. In all such flows, however, trade-offs between differing stress generation mechanisms are summarized by variations in N_S, N_B, and related dimensionless parameters (Table 1).

Evaluation of stress regimes in terms of N_S and N_B must also take account of the fact that the effective viscosity μ and density ρ_f of the fluid phase may be increased by the presence of fine particles carried in suspension. Mechanically, these fine particles may be regarded as part of the fluid phase rather than solid phase if the time required for "Stokesian" settling of the particles (viscous settling in the absence of interaction with other particles) exceeds the flow duration. By this rationale, particles that are silt-sized and smaller can be viewed as part of the fluid phase in many water-saturated debris flows [*Iverson*, 1997a]. Larger particles constitute the granular solids.

Trade-offs between stress generation by intergranular friction, intergranular collisions, and viscous fluid flow have three important implications for the Coulomb mixture model that we develop here.

1. For gravity-driven flows with free supper surfaces the nearly constant relationship between intergranular shear and normal stresses in friction-dominated and collision-dominated flows extends a key feature of Coulomb behavior beyond the slow-flow regime where Coulomb friction clearly dominates.

2. Individual flows may contain regions in which different stress generation mechanisms dominate. For example, data

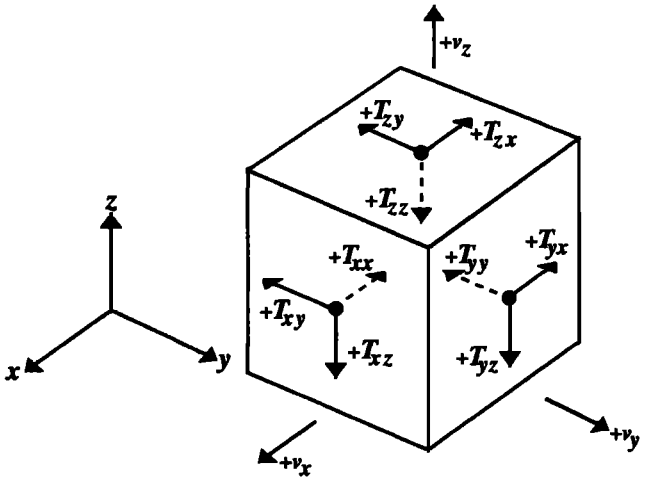

Figure 2. Definitions of the right-handed local coordinate system and sign conventions used to calculate stresses and velocities. The z coordinate is an outward directed vector normal to the bed. The x and y coordinates are oriented orthogonally but otherwise arbitrarily in the plane normal to z. Normal stress components (indicated by dashed arrows) are positive in compression, and both shear and normal stress components are positive when oriented as shown.

from debris flows [*Iverson*, 1997a; *Major and Iverson*, 1999] and observations of pyroclastic flows [*Rowley et al.*, 1981; *Wilson and Head*, 1981] indicate that fine-grained flow interiors can remain mostly fluidized, while coarse-grained flow perimeters exhibit much frictional strength.

3. Lack of rate-dependent stresses implied by Coulomb friction does not eliminate rate dependence in a mixture of Coulomb solids and fluid, provided the fluid has nonzero viscosity. The degree of rate dependence in such mixtures depends on the degree to which fluid pressures reduce intergranular Coulomb friction and transfer shear stresses to the fluid phase.

3. Mixture Theory Framework

To describe flowing grain-fluid mixtures, we adopt mass and linear momentum balances from continuum mixture theory, which postulates that separate but strongly coupled equations describe motion of the solid and fluid constituents [e.g., *Atkin and Craine*, 1976]. Angular momentum equations can also be formulated but are unnecessary if stress tensors are symmetric. Separate energy balance equations are unnecessary because we assume the mixture is isothermal. Addition of the equations for the solid and fluid constituents yields mass and momentum conservation equations applicable to the mixture as a whole [*Iverson*, 1997a]:

$$\partial\rho/\partial t + \nabla\cdot(\rho\mathbf{v}) = 0 \tag{4}$$

$$\rho(\partial\mathbf{v}/\partial t + \mathbf{v}\cdot\nabla\mathbf{v}) = -\nabla\cdot(\mathbf{T}_s + \mathbf{T}_f + \mathbf{T}') + \rho\mathbf{g} \tag{5}$$

in which

$$\rho = \rho_s\upsilon_s + \rho_f\upsilon_f \tag{6}$$

$$\mathbf{v} = (\rho_s\upsilon_s\mathbf{v}_s + \rho_f\upsilon_f\mathbf{v}_f)/\rho \tag{7}$$

Here ρ is mass density, t is time, $\mathbf{v}$ is velocity, υ is volume fraction, $\mathbf{g}$ is gravitational acceleration, $\mathbf{T}$ is stress, and normal stresses are defined as positive in compression (Figure 2). Quantities with subscript s refer to the solid phase, those with subscript f refer to the fluid phase, and those with no subscript refer to the solid-fluid mixture. The quantity $\mathbf{T}'$ is a contribution to the mixture stress that results from motion of the solid and fluid constituents relative to the mixture as a whole, and is defined by a sum of dyadic products:

$$\mathbf{T}' = -\rho_s\upsilon_s(\mathbf{v}_s - \mathbf{v})(\mathbf{v}_s - \mathbf{v}) - \rho_f\upsilon_f(\mathbf{v}_f - \mathbf{v})(\mathbf{v}_f - \mathbf{v}). \tag{8}$$

This stress arises from the nonlinear convective acceleration terms in the momentum balances for the individual solid and fluid constituents, which do not sum to yield the mixture convective acceleration $\mathbf{v}\cdot\nabla\mathbf{v}$.

Mixture theory equations hold several advantages over equations that treat grain-fluid mixtures as single-phase continua. First, they account explicitly for solid and fluid volume fractions and velocities and for their influence on flow dynamics. Second, they include explicit dependence on solid- and fluid-phase stresses and thereby eliminate the need for an amalgamated stress tensor that lumps the effects of solid and fluid constituents and their interactions. Third, they subsume standard quasi-static theories of slope failure (commonly triggered by rising pore fluid pressure) and sediment consolidation (diffusion of pore fluid pressure) as special cases. Thus mixture theory provides a unified framework for analyzing grain-fluid flows with differing compositions and behaviors, from flow initiation to deposit consolidation.

Explicit evaluation of the stress $\mathbf{T}'$ defined in (8) can be avoided by using an approximation suitable for many geophysical flows. The approximation results from considering the motion of the pore fluid in a frame of reference that moves with the solid phase, just as in standard porous media problems. With that rationale, we define the specific discharge of fluid $\mathbf{q}_f$ relative to the solids as $\mathbf{q}_f/\upsilon_f = \mathbf{v}_f - \mathbf{v}_s$ [cf. *Bear*, 1972]. Following *Iverson* [1997a, p. 281], we note that if $|\mathbf{q}_f/\upsilon_f| \ll |\mathbf{v}_s|$ and ρ_s, ρ_f and ρ are constant, the mixture theory mass and momentum balance equations reduce to the simplified forms

$$\nabla\cdot\mathbf{v}_s = 0 \tag{9}$$

$$\rho(\partial\mathbf{v}_s/\partial t + \mathbf{v}_s\cdot\nabla\mathbf{v}_s) = -\nabla\cdot(\mathbf{T}_s + \mathbf{T}_f) + \rho\mathbf{g}, \tag{10}$$

in which $\mathbf{T}_s + \mathbf{T}_f$ is the total stress in the mixture. Physically, (9) and (10) assume that motion of fluid relative to the solids is so slow that fluid velocities and accelerations differ negligibly from those of adjacent solids and that the mixture density ρ is essentially constant. The equations differ from those describing motion of the solids alone because they include the effects of the mixture density and fluid stress. Emphasis on the motion of the granular solids is appropriate for geophysical flows in which the presence of pore fluid may be transitory; after a deposit of such a flow is emplaced and consolidated, the geologic record of the event includes only the static solids.

Because the validity of the simplification in (9) and (10) requires $|\mathbf{q}_f|/|\upsilon_f\mathbf{v}_s| \ll 1$, we evaluate this quantity by considering the pertinent scales for $|\mathbf{q}_f|$ and $|\mathbf{v}_s|$. For $|\mathbf{v}_s|$ the pertinent scale (or upper bound) is the velocity of a freely falling body because the potential for free fall drives downslope motion of the granular mass [*Savage and Hutter*, 1989; *Iverson*, 1997a, 1997b]. Therefore $|\mathbf{v}_s|$ scales with $\sqrt{gL}$, where L is the flow length (typically similar to the slope height for flows on steep slopes) and g is the magnitude of $\mathbf{g}$. An appropriate scale for $|\mathbf{q}_f|$ is the specific discharge necessary to fluidize or liquefy the granular mass; if $|\mathbf{q}_f|$ exceeds this threshold, the mass may disaggregate and lose the character of a coherent mixture.

The threshold for fluidization can be estimated by reckoning that it implies a slope-normal pore pressure gradient $\partial p/\partial z$ that balances the z component of the total mixture weight per unit volume, $\partial p/\partial z = -\rho g_z$ [*Gidaspow*, 1994]. Note that we define g_s as positive, although g_z acts in the direction of $-z$ (Figure 3). The gradient $\partial p/\partial z$ is related to $|\mathbf{q}_f|$ by Darcy's law for fluid flow in the positive z (upward) direction, $|\mathbf{q}_f| = -(k/\mu)(\partial p/\partial z + \rho_f g_z)$, where k is the intrinsic permeability of the granular mass and μ is the pore fluid viscosity [*Bear*, 1972]. Substituting $\partial p/\partial z = -\rho g_z$ into Darcy's law and simplifying the resulting expression yields the fluidization threshold $|\mathbf{q}_f| = (k/\mu)(\rho_s - \rho_f)v_s g_z$.

The ratio of the fluidization scale for $|\mathbf{q}_f|$ and the velocity scale for $|v_f \mathbf{v}_s|$ yields the dimensionless number

$$N_f \equiv \frac{|\mathbf{q}_f|}{|v_f \mathbf{v}_s|} = \frac{k}{\mu}\frac{v_s}{v_f}(\rho_s - \rho_f)\sqrt{g/L}, \tag{11}$$

which assumes for simplicity that $g_z \approx g$. Table 1 lists typical values of N_f for geophysical grain-fluid flows. The values demonstrate that $N_f \ll 1$ probably applies in most such flows and thereby support the validity of the simplified equations of motion (equations (9) and (10)). A condition of full fluidization (which can obtain even if $|\mathbf{q}_f| = 0$ for the limiting case $\rho_s = \rho_f$ investigated by *Bagnold* [1954]) does not generally invalidate the simplified equations. However, full fluidization does imply that solid-phase stresses result from momentum exchange by grain collisions rather than from Coulomb friction.

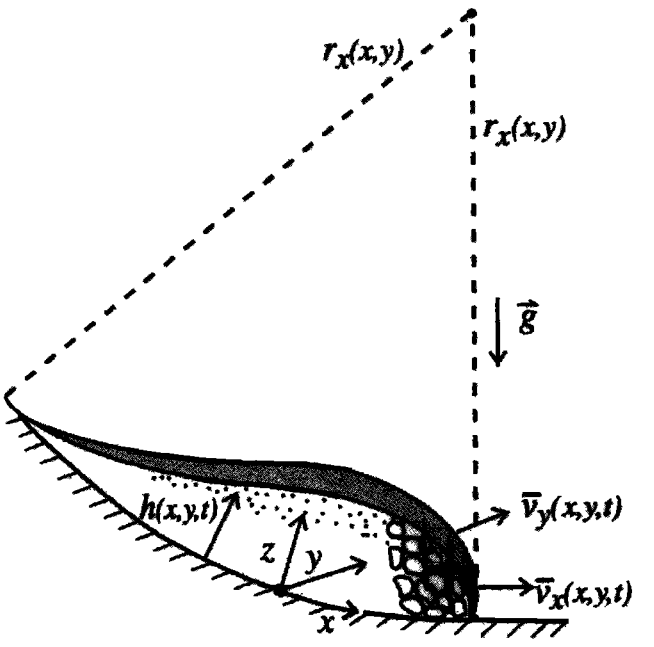

Figure 3. Schematic cut-away view of an unsteady flow down a curvilinear slope, illustrating the local coordinate system and dependent variables $h(x, y, t)$, $\bar{v}_x(x, y, t)$, $\bar{v}_y(x, y, t)$ that describe depth-averaged flow. The x component of bed curvature is specified by the local radius of curvature r_x.

4. Depth-Averaged Theory

A key step in further simplifying the equations of motion involves depth averaging to eliminate explicit dependence on the coordinate normal to the bed, z. Depth averaging requires decomposing the vector equations (9) and (10) into component equations in locally defined x-y-z orthogonal directions, then integrating each component equation from the base of the flow at $z = 0$ to the surface of the flow at $z = h$ (Figure 3). The pertinent mathematical manipulations are rather lengthy, and we omit some details here. However, the details are similar to those in *Vreugdenhil*'s [1994] derivation of the standard shallow water equations and in *Gray et al.*'s [1999] derivation of dry granular avalanche equations. The derivation makes frequent use of Leibniz' theorem for interchanging the order of integrations and differentiations [*Abramowitz and Stegun*, 1964, p. 11] and of kinematic boundary conditions that specify that mass neither enters nor leaves at the free surface or base of the flow:

$$\frac{\partial h}{\partial t} + v_x\frac{\partial h}{\partial x} + v_y\frac{\partial h}{\partial y} - v_z = 0 \qquad z = h(x, y, t) \tag{12}$$

$$v_z = 0 \qquad z = 0. \tag{13}$$

In (12), (13), and equations hereinafter, all v denote the solid-phase velocity, and subscripts x, y, and z denote Cartesian components of vector and tensor quantities. Depth averaging also implies that the total normal stress (the sum of solid and fluid normal stresses) in the z direction balances the z component of the mixture weight:

$$T_{s(zz)} + T_{f(zz)} = (h - z)\rho g_z. \tag{14}$$

Equation (14), in turn, leads to expressions for the total normal stress at the bed and for the depth-averaged total normal stress in the z direction,

$$T_{s(zz)}|_{z=0} + T_{f(zz)}|_{z=0} = \rho g_z h \tag{15}$$

$$\bar{T}_{s(zz)} + \bar{T}_{f(zz)} = \frac{1}{h}\int_0^h \rho g_z(h - z)\,dz = \tfrac{1}{2}\rho g_z h. \tag{16}$$

In (15), (16), and equations hereinafter, overbars denote depth-averaged quantities defined by integrals similar to that in (16). Thus depth-averaged velocities are defined by

$$\bar{v}_x = \frac{1}{h}\int_0^h v_x\,dz \qquad \bar{v}_y = \frac{1}{h}\int_0^h v_y\,dz \tag{17}$$

and depth-averaged stress components (denoted generically by subscript ij) are defined by

$$\bar{T}_{ij} = \frac{1}{h}\int_0^h T_{ij}\,dz. \tag{18}$$

Using these definitions together with (9) and (10), we obtain depth-averaged mass and momentum conservation equations for motion in the x and y directions:

$$\frac{\partial h}{\partial t} + \frac{\partial(h\bar{v}_x)}{\partial x} + \frac{\partial(h\bar{v}_y)}{\partial y} = 0 \tag{19}$$

$$\rho\left[\frac{\partial(h\bar{v}_x)}{\partial t} + \frac{\partial(h\bar{v}_x^2)}{\partial x} + \frac{\partial(h\bar{v}_x\bar{v}_y)}{\partial y}\right] = -\int_0^h\left[\frac{\partial T_{s(xx)}}{\partial x} + \frac{\partial T_{f(xx)}}{\partial x} + \frac{\partial T_{s(yx)}}{\partial y} + \frac{\partial T_{f(yx)}}{\partial y} + \frac{\partial T_{s(zx)}}{\partial z} + \frac{\partial T_{f(zx)}}{\partial z} - \rho g_x\right]dz \tag{20}$$

$$\rho\left[\frac{\partial(h\bar{v}_y)}{\partial t}+\frac{\partial(h\bar{v}_y^2)}{\partial y}+\frac{\partial(h\bar{v}_y\bar{v}_x)}{\partial x}\right]=-\int_0^h\left[\frac{\partial T_{s(yy)}}{\partial y}+\frac{\partial T_{f(yy)}}{\partial y}\right.$$

$$\left.+\frac{\partial T_{s(xy)}}{\partial x}+\frac{\partial T_{f(xy)}}{\partial x}+\frac{\partial T_{s(zy)}}{\partial z}+\frac{\partial T_{f(zy)}}{\partial z}-\rho g_y\right]dz \qquad (21)$$

The factor h that appears explicitly or implicitly in each term of these equations can be eliminated from the left-hand side of (20) and (21) by combining these equations with (19) [cf. *Iverson*, 1997b]. However, here we retain the factor h so that individual terms have "conservative" forms that represent fluxes of mass or momentum insofar as possible [cf. *Vreugdenhil*, 1994]. Conservative forms offer significant advantages in our numerical solution technique [*Denlinger and Iverson*, this issue].

4.1. Evaluation of Solid Stresses

We assume that wherever bulk deformation occurs, the solid-phase stress obeys the Coulomb rule (2a), (2b), and (2c) with $c = 0$. The assumption $c = 0$ is generally appropriate for granular solids undergoing large deformations that rupture cohesive bonds [*Skempton*, 1985; *Duran*, 2000]. Relationships between the solid stress $\mathbf{T}_s$, total mixture stress $\mathbf{T}_s + \mathbf{T}_f$, and effective stress $\mathbf{T}_e$ are described by $\mathbf{T}_s + \mathbf{T}_f = \mathbf{T}_e + \mathbf{I}p + v_f\mathbf{T}_{fvis}$, where $\mathbf{T}_e$ and p are the conventional intergranular effective stress and pore fluid pressure, $\mathbf{I}$ is the identity tensor, and $\mathbf{T}_{fvis}$ is the deviatoric stress due to viscous fluid flow [cf. *Iverson*, 1997a]. In mixture theories it is common to define the fluid stress as $\mathbf{T}_f = v_f(\mathbf{I}p + \mathbf{T}_{fvis})$ and solid stress as $\mathbf{T}_s = \mathbf{T}_e + v_s\mathbf{I}p$. However, to streamline our formulation and make it comparable to that of conventional soil mechanics, we define the fluid stress as $\mathbf{T}_f = \mathbf{I}p + v_f\mathbf{T}_{fvis}$ and equate the solid stress and effective stress, $\mathbf{T}_s = \mathbf{T}_e$. Either set of stress definitions is satisfactory in our depth-averaged model. Either set of definitions yields the same total mixture stress and same depth-averaged momentum equation for the mixture as a whole.

Coulomb stresses in a pervasively deforming granular material may be very complicated in detail, but our use of depth-averaged equations of motion indicates that a commensurately simple treatment of stresses is appropriate [*Savage and Hutter*, 1989; *Gray et al.*, 1999]. Therefore we use a "uniform slab" approximation, which assumes that stresses at any location and time (x, y, z, t) depend only on the local thickness, $h(x, y, t)$ and not on thickness gradients $\partial h/\partial x$ and $\partial h/\partial y$. Despite this approximation, thickness gradients influence the overall momentum balance, because all stress components are differentiated in space and multiplied by h as a result of the mathematical operations in (20) and (21).

Before evaluating Coulomb stress components, we replace the local solid stresses in (20) and (21) with depth-averaged stresses and basal shear stresses obtained by evaluating the integrals on the right-hand sides of (20) and (21) and using Leibniz' theorem to simplify the resulting expression. For (20) we find

$$-\int_0^h\left[\frac{\partial T_{s(xx)}}{\partial x}+\frac{\partial T_{s(yx)}}{\partial y}+\frac{\partial T_{s(zx)}}{\partial z}\right]dz$$

$$=-\frac{\partial(h\bar{T}_{s(xx)})}{\partial x}-\frac{\partial(h\bar{T}_{s(yx)})}{\partial y}+T_{s(zx)}|_{z=0}, \qquad (22)$$

and we find an analogous expression (with x and y interchanged) for (21).

Evaluation of individual Coulomb stress components follows a rationale like that in *Iverson*'s [1997a] two-dimensional analysis, with one important complication: whereas a depth-averaged two-dimensional stress field involves no transverse shear stresses ($\bar{T}_{s(yx)}$, $\bar{T}_{s(xy)}$), such shear stresses appear in both the x and y direction momentum equations used here. Moreover, these conjugate shear stresses must satisfy $\bar{T}_{s(yx)} = \bar{T}_{s(xy)}$ to maintain the stress symmetry that preserves mechanical equilibrium in the x-y plane. This shear stress symmetry also requires equality of the depth-averaged intergranular normal stresses $\bar{T}_{s(xx)}$ and $\bar{T}_{s(yy)}$ because shear stresses are proportional to normal stresses in deforming Coulomb materials.

Following *Savage and Hutter* [1989, 1991], *Gray et al.* [1999], and *Iverson* [1997a, 1997b], we relate the depth-averaged normal stresses $\bar{T}_{s(xx)}$ and $\bar{T}_{s(yy)}$ to the depth-averaged z direction normal stress $\bar{T}_{s(zz)}$ by using a lateral stress coefficient, $k_{act/pass}$, derived from Coulomb theory

$$\bar{T}_{s(xx)} = \bar{T}_{s(yy)} = k_{act/pass}\bar{T}_{s(zz)}. \qquad (23)$$

Unlike *Gray et al.* [1999], however, we use a scalar lateral stress coefficient, which applies in the x and y directions simultaneously. Use of a scalar coefficient ensures frame invariance in the x-y plane and preserves the stress symmetry $\bar{T}_{s(yx)} = \bar{T}_{s(xy)}$ described above, whereas use of multiple coefficients may violate invariance and symmetry.

At each point in a flow, our model stipulates that one of three deterministic values of the lateral stress coefficient applies. The coefficient values where the depth-averaged flow locally diverges (indicated by $\partial\bar{v}_x/\partial x + \partial\bar{v}_y/\partial y > 0$) or converges (indicated by $\partial\bar{v}_x/\partial x + \partial\bar{v}_y/\partial y < 0$) are given by

$$k_{act/pass} = 2\,\frac{1 \mp [1 - \cos^2\varphi_{int}(1 + \tan^2\varphi_{bed})]^{1/2}}{\cos^2\varphi_{int}} - 1 \qquad (24)$$

in which "$-$" in "$\mp$" applies to the "active" coefficient for diverging flow, k_{act}, and "$+$" applies to the "passive" coefficient for converging flow, k_{pass}. These coefficient definitions are more general than those of classical Rankine earth pressure coefficients commonly used in soil mechanics [*Rankine*, 1857] because (24) is derived by assuming that Coulomb failure occurs simultaneously along the bed (where $\varphi = \varphi_{bed}$) and within the overlying sediment mixture (where $\varphi = \varphi_{int}$) [*Iverson*, 1997a]. For the special case in which $\varphi_{bed} = 0$, the coefficient definitions in (24) reduce to the classical Rankine definitions [e.g., *Lambe and Whitman*, 1979]. For most values of φ_{bed}, corresponding values of $k_{act/pass}$ indicate that lateral stresses in regions of converging flow exceed bed-normal stresses, whereas lateral stresses in regions of diverging flow are less than bed-normal stresses (Figure 4). Lateral normal stresses where flow converges typically exceed those where flow diverges by a factor of 2 to 10. An exception to this behavior occurs if the bed has maximum roughness, in which case, $\varphi_{bed} = \varphi_{int}$ and (24) reduces to a single-valued expression:

$$k_{act/pass} = \frac{1 + \sin^2\varphi_{int}}{1 - \sin^2\varphi_{int}}. \qquad (25)$$

The uniqueness of this value indicates that a slab of Coulomb material can move downslope with zero velocity divergence (implying no thinning or thickening) only if the bed friction angle equals the internal friction angle.

A different value of $k_{act/pass}$ applies if Coulomb failure does not occur and the sediment mixture is static. In this case,

stresses are insufficient for full mobilization of frictional forces, and friction angles do not determine the stress state. We approximate this statically indeterminate stress state by assuming that $k_{\text{act/pass}} = 1$, and consequently, $\bar{T}_{s(xx)} = \bar{T}_{s(yy)} = \bar{T}_{s(zz)}$. Alternative assumptions about the static stress state are possible [e.g., *Reid and Iverson*, 1992], but none appears more strongly warranted than the simple assumption $k_{\text{act/pass}} = 1$. The ramifications of this assumption are clarified below, where we describe solutions of the governing equations for static problems.

We express the depth-averaged lateral stresses in the granular solids by combining (23) and (16) to obtain

$$\bar{T}_{s(xx)} = \bar{T}_{s(yy)} = k_{\text{act/pass}}(\tfrac{1}{2}\rho g_z h - \bar{T}_{f(zz)}), \tag{26}$$

and we evaluate the depth-averaged fluid normal stress $\bar{T}_{f(zz)}$ in (26) by identifying this stress as the pore fluid pressure. We assume that the pore fluid pressure varies linearly from a maximum of p_{bed} at the base of the flow to zero (i.e., atmospheric reference pressure) at the flow surface, yielding

$$\bar{T}_{f(zz)} = \frac{1}{h}\int_0^h T_{f(zz)}\,dz = \tfrac{1}{2}T_{f(zz)}|_{z=0} = \tfrac{1}{2}p_{\text{bed}}. \tag{27}$$

The assumption of linear variation of fluid pressure is appropriate because nonlinear variation would imply locally unbalanced forces in the z direction, violating the static force balance in (14). Linear variation of fluid pressure also allows us to express the fluid pressure as a fraction λ of the total basal normal stress given by (15), yielding

$$p_{\text{bed}} = \lambda\rho g_z h. \tag{28}$$

This definition, similar to that of *Hubbert and Rubey* [1959], aids brevity and indicates that $\lambda = 1$ represents a case of zero basal effective stress or complete liquefaction. Combining (26), (27), and (28) yields the expression we use for the solid lateral normal stresses:

$$\bar{T}_{s(xx)} = \bar{T}_{s(yy)} = k_{\text{act/pass}}[\tfrac{1}{2}\rho g_z h(1-\lambda)]. \tag{29}$$

Next, we derive an expression for the transverse solid shear stresses $\bar{T}_{s(yx)}$, $\bar{T}_{s(xy)}$ by first noting that equality of $\bar{T}_{s(xx)}$ and $\bar{T}_{s(yy)}$ implies that these depth-averaged normal stresses equal the mean normal stress in the x-y plane. Moreover, the stresses $\bar{T}_{s(xx)}$ and $\bar{T}_{s(yy)}$ act on conjugate planes of maximum shear, as demonstrated by the equivalence of (2b) and (2c). Consequently, (2b) gives the form of the Coulomb rule applicable on these planes, and we combine (2b) with (29) to obtain the shear stress equation:

$$\bar{T}_{s(yx)} = \bar{T}_{s(xy)} = -\text{sgn}\,(\partial\bar{v}_x/\partial y) \cdot\{k_{\text{act/pass}}[\tfrac{1}{2}\rho g_z h(1-\lambda)]\}\sin\varphi_{\text{int}}. \tag{30}$$

Here we introduce the factor $-\text{sgn}\,(\partial\bar{v}_x/\partial y)$ to designate the sign (+ or −) opposite that of the argument $\partial\bar{v}_x/\partial y$, which ensures that shear stresses oppose shear straining in the x-y plane (see Figures 2 and 3).

Basal sliding necessarily accompanies bulk mixture motion unless $\varphi_{\text{bed}} \geq \varphi_{\text{int}}$ and frictional locking occurs at the bed. We evaluate solid shear stresses at the bed by combining (28) with the Coulomb equation for basal sliding (2a) and the equation for the z direction normal stress at the bed (15), which yields

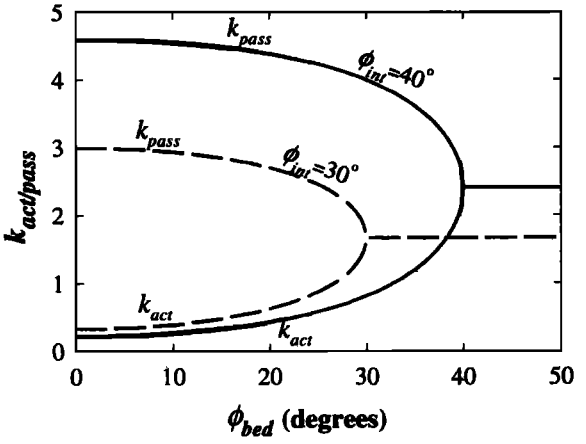

Figure 4. Graphs of the active and passive lateral stress coefficients calculated from equation (24). Graphs depict values of k_{act} and k_{pass} as functions of φ_{bed}, for two typical values of φ_{int}. If $\varphi_{\text{bed}} \geq \varphi_{\text{int}}$, the graphs show that $k_{\text{act/pass}}$ has a unique value, given by equation (25). In such cases, frictional locking occurs at the bed, and all slip occurs internally.

$$T_{s(zx)}|_{z=0} = -\text{sgn}\,(\bar{v}_x)[\rho g_z h(1-\lambda)]\tan\varphi_{\text{bed}} \tag{31a}$$

and an analogous equation for $T_{s(zy)}|_{z=0}$. In these equations, factors of the form $-\text{sgn}\,(\bar{v}_x)$ stipulate that basal Coulomb stresses oppose basal sliding. These sign factors are exactly analogous to that in (30) but involve only the pertinent velocity component (rather than its gradient) because velocity gradients in the z direction do not appear in the depth-averaged model.

Resistance due to basal sliding friction is modified by changes in bed slope that affect the apparent weight of the moving mass. For example, where the bed slope decreases in the downstream direction, part of the depth-averaged momentum flux per unit area $\rho\bar{v}_x^2$ is directed into the bed and resisted by the reaction force provided by the underlying Earth (assumed to be infinitely massive and immobile). This external reaction force redirects the flow's depth-averaged momentum flux to keep it parallel to the bed. However, the action-reaction at the bed also locally increases the normal stress at the bed by an amount $(\rho h\bar{v}_x^2)/r_x$, where r_x is the radius of local bed curvature in the x direction and $\bar{v}_x^2/r_x$ is the associated centripetal acceleration (Figure 3). Thus, for curving beds, (31a) generalizes to

$$T_{s(zx)}|_{z=0} = -\text{sgn}\,(\bar{v}_x)\left[\rho g_z h(1-\lambda)\left(1+\frac{\bar{v}_x^2}{r_x g_z}\right)\right]\tan\varphi_{\text{bed}}. \tag{31b}$$

Equation (31b) reduces to (31a) in the limit $r_x \to \infty$ applicable to planar beds, and it applies to both bed concavities with positive curvature ($r_x > 0$) and bed convexities with negative curvature ($r_x < 0$). (For combinations of velocity and convex curvature that satisfy $\bar{v}_x^2 = -r_x g_z$, (31b) implies that bed friction vanishes because the mass becomes effectively weightless as it descends in free fall.) *Savage and Hutter* [1991] and *Gray et al.* [1999] obtained results like (31b) through formal transformations from linear to curvilinear coordinates. Their scaling analyses demonstrated that other terms generated by such coordinate transformations are generally negligible. Consequently, (31b) contains the only term we use for adapting (19), (20), and (21) to curving terrain.

4.2. Evaluation of Fluid Stresses

We assume that fluid-phase stresses in (20) and (21) obey the conventional linear law that governs the behavior of Newtonian fluids (e.g., water). Fluid stresses include both an isotropic pressure component that not does not depend on viscous deformation (as used in (27)) and a deviatoric, viscous component [e.g., *Bird et al.*, 1960; *Schlichting*, 1979]. More complicated, non-Newtonian fluid stresses could be included instead, but no compelling data indicate that this complication is warranted.

To streamline our presentation, we take advantage of results well-known from derivations of the standard Navier-Stokes equations for flow of incompressible Newtonian fluids [e.g., *Bird et al.*, 1960; *Schlichting*, 1979]. Adapting the Navier-Stokes equations, we find that the fluid stress terms in (20) can be expressed by

$$-\int_0^h \left[\frac{\partial T_{f(xx)}}{\partial x} + \frac{\partial T_{f(yx)}}{\partial y} + \frac{\partial T_{f(zx)}}{\partial z}\right] dz$$

$$= -\int_0^h \left[\frac{\partial p}{\partial x} - v_f\mu\left(\frac{\partial^2 v_x}{\partial x^2} + \frac{\partial^2 v_x}{\partial y^2} + \frac{\partial v_x^2}{\partial z^2}\right)\right] dz, \qquad (32)$$

and we find an analogous expression for fluid stresses in (21). As discussed during evaluation of solid stresses, we multiply the pore fluid viscosity μ by the fluid volume fraction v_f because only this fraction of the mixture produces viscous stresses.

Consistent with (27) and (28), we assume that the fluid pressure in (32) varies linearly from a maximum of p_{bed} at the bed to zero at the free surface. Using this assumption and Leibniz' theorem, we integrate the pressure term in (32) directly, yielding

$$-\int_0^h \frac{\partial p}{\partial x}\, dz = -\frac{\partial}{\partial x}\int_0^h \lambda\rho g_z(h - z)\, dz$$

$$= -\lambda\rho g_z h\,\frac{\partial h}{\partial x} = -h\,\frac{\partial p_{\text{bed}}}{\partial x}. \qquad (33)$$

Equation (33) establishes the relationship between longitudinal fluid pressure gradients and their representation in the depth-averaged model.

Similarly, term-by-term integration of the velocity derivatives on the right-hand side of (32) establishes the relationship between viscous stress gradients and their depth averages. For example, using Leibniz' theorem and some algebraic manipulation, we find that the term involving $\partial^2 v_x/\partial x^2$ in (32) can be written as

$$\int_0^h v_f\mu\,\frac{\partial^2 v_x}{\partial x^2}\, dz = v_f\mu\left[h\,\frac{\partial^2 \bar{v}_x}{\partial x^2} + 2\,\frac{\partial}{\partial x}\left(\bar{v}_x - v_x(h)\right)\frac{\partial h}{\partial x}\right.$$

$$\left. + \left(\bar{v}_x - v_x(h)\right)\frac{\partial^2 h}{\partial x^2}\right], \qquad (34)$$

where $v_x(h)$ specifies the value of v_x at the flow surface. An equation analogous to (34) results from integration of the viscous term involving $\partial^2 v_x/\partial y^2$ in (32). Employing the same uniform-slab approximation ($\partial h/\partial x = 0$) used to derive the Coulomb stress equations, the right-hand side of (34) simplifies and reduces the equation to

$$\int_0^h v_f\mu\,\frac{\partial^2 v_x}{\partial x^2}\, dz = v_f\mu h\,\frac{\partial^2 \bar{v}_x}{\partial x^2}. \qquad (35)$$

The same simplification reduces the analogous equation for $\partial^2 v_x/\partial y^2$ to

$$\int_0^h v_f\mu\,\frac{\partial^2 v_x}{\partial y^2}\, dz = v_f\mu h\,\frac{\partial^2 \bar{v}_x}{\partial y^2}. \qquad (36)$$

The final viscous stress term in (32) can be integrated directly, yielding

$$\int_0^h v_f\mu\,\frac{\partial^2 v_x}{\partial z^2}\, dz = v_f\mu\left[\left.\frac{\partial v_x}{\partial z}\right|_{z=h} - \left.\frac{\partial v_x}{\partial z}\right|_{z=0}\right] = -3v_f\mu\,\frac{\bar{v}_x}{h}. \qquad (37)$$

The last form of this equation results from assuming a no-slip basal boundary condition for fluid flow and a parabolic velocity profile in the z direction [cf. *Bird et al.*, 1960, pp. 37–40]. Velocity profiles with different shapes would yield numerical coefficients different from 3 in this expression but would not otherwise change its form [cf. *Iverson*, 1997a, 1997b].

Combination of the results from (32) through (37) indicates that the depth-averaged fluid stress terms in (20) can be represented by

$$-\int_0^h \left[\frac{\partial T_{f(xx)}}{\partial x} + \frac{\partial T_{f(yx)}}{\partial y} + \frac{\partial T_{f(zx)}}{\partial z}\right] dz = -h\,\frac{\partial p_{\text{bed}}}{\partial x} + v_f\mu h\,\frac{\partial^2 \bar{v}_x}{\partial x^2}$$

$$+ v_f\mu h\,\frac{\partial^2 \bar{v}_x}{\partial y^2} - 3v_f\mu\,\frac{\bar{v}_x}{h}. \qquad (38)$$

An analogous expression (with x and y interchanged) represents the fluid stress terms in (21).

4.3. Governing Equations

The final form of the depth-averaged x direction momentum equation results from combining (18) and (20) with (26), (27), (28), (29), (30), (31b), and (38) and using the substitution $\partial(h^2/2)/\partial x = h(\partial h/\partial x)$ to eliminate explicit dependence on h^2. After this elimination, (28) may be used to eliminate λ in favor of p_{bed}, which improves physical clarity. The final result is the x momentum equation

$$\rho\left[\frac{\partial(h\bar{v}_x)}{\partial t} + \frac{\partial(h\bar{v}_x^2)}{\partial x} + \frac{\partial(h\bar{v}_x\bar{v}_y)}{\partial y}\right]$$

$$= -\text{sgn}\,(\bar{v}_x)(\rho g_z h - p_{\text{bed}})\left(1 + \frac{\bar{v}_x^2}{r_x g_z}\right)\tan\varphi_{\text{bed}} - 3v_f\mu\,\frac{\bar{v}_x}{h}$$

$$- hk_{\text{act/pass}}\,\frac{\partial}{\partial x}\left(\rho g_z h - p_{\text{bed}}\right) - h\,\frac{\partial p_{\text{bed}}}{\partial x} + v_f\mu h\,\frac{\partial^2 \bar{v}_x}{\partial x^2}$$

$$- \text{sgn}\left(\frac{\partial \bar{v}_x}{\partial y}\right)hk_{\text{act/pass}}\,\frac{\partial}{\partial y}\left(\rho g_z h - p_{\text{bed}}\right)\sin\varphi_{\text{int}}$$

$$+ v_f\mu h\,\frac{\partial^2 \bar{v}_x}{\partial y^2}$$

$$+ \rho g_x h. \qquad (39)$$

The y direction momentum equation is obtained by interchanging x and y in (39).

Terms on the right-hand side of (39) are grouped by line according to type of stress: the first line represents basal shear stresses, the second line represents longitudinal normal stresses, the third and fourth lines represent transverse shear stresses, and the fifth line represents the driving stress due to the gravitational body force. Combined with the mass balance equation (19), equation (39) and its y direction analog provide a set of three governing equations in three unknowns, $\bar{v}_x(x, y, t)$, $\bar{v}_y(x, y, t)$, and $h(x, y, t)$, which we use to compute flows of dense solid-fluid mixtures. An additional equation (described below) governs evolution of p_{bed}.

Importantly, (39) and its y direction analog are invariant with respect to rotation of the x and y coordinates about the z axis. This frame invariance is crucial if the equations are used to solve problems involving motion over irregular topography, for which flow paths are unknown a priori.

Examination of limiting cases reveals another key feature of our governing equations. For cases in which no pore fluid pressure or viscosity are present, the equations reduce to a set applicable to granular avalanches with purely frictional energy dissipation. At the other extreme, for cases in which the mass is fully liquefied by persistent high pore fluid pressure ($p_{bed} = \rho g_z h$), the equations reduce to a set applicable to Newtonian fluid flow with purely viscous dissipation. For intermediate cases the equations indicate a combination of frictional and viscous energy dissipation that changes in response to spatial and temporal changes in pore pressure. Before we consider pore pressure evolution, however, we describe initial and boundary conditions for the governing mass and momentum conservation equations, and we derive analytical solutions for some simple problems in which pore pressure evolution is neglected.

4.4. Initial and Boundary Conditions

To solve the governing equations, we use initial conditions that specify zero flow velocity and an initial thickness distribution, $h_0(x, y)$,

$$\bar{v}_x(x, y, 0) = \bar{v}_y(x, y, 0) = 0 \quad h(x, y, 0) = h_0(x, y). \tag{40}$$

These conditions represent a static mass of specified volume and geometry that is poised to descend a slope. In principle, we could use the static limits of our model equations to identify sectors of a landscape where a sloping mass has reached Coulomb equilibrium and imminent failure, but we have not yet implemented a search algorithm to perform this task. We consider this issue again where we describe analytical solutions for static problems.

We use boundary conditions that specify the flow thickness is zero at coordinates that denote the margins (x_M, y_M) of the flowing mass,

$$h(x_M, y_M, t) = 0. \tag{41}$$

These conditions are connected to the velocities at the flow margins by

$$\bar{v}_x(x_M, y_M, t) = dx_M/dt \qquad \bar{v}_y(x, y_M, t) = dy_M/dt. \tag{42}$$

5. Analytical Solutions

Solutions of nonlinear, hyperbolic equations such as (39) generally demand special numerical methods [*Denlinger and Iverson*, this issue], but exact analytical solutions can be obtained for some significant special cases. In the cases that we consider, the mass balance equation (19) is satisfied trivially, the y momentum balance is immaterial, and the x momentum balance simplifies substantially. In some special cases, analytical solutions predict phenomena observable in the field, and in all cases they aid comparison with other models and help to test the veracity of numerical results.

5.1. Unsteady, Translational Motion

Unsteady motion of an uniform mass descending a slope illustrates some elementary but important features of Coulomb mixture motion and reveals a strong but superficial resemblance between the mixture model and the generalized Bingham (Coulomb viscous) model of *Johnson* [1970]. If a homogenous mass of Coulomb mixture with uniform thickness $h = H$ moves downslope with no velocity gradients in the x and y directions, the depth-averaged x momentum equation (39) reduces to a simple linear equation describing translational motion:

$$\rho \frac{d(H\bar{v}_x)}{dt} = -(\rho g_z H - p_{bed}) \tan \varphi_{bed} - 3\nu_f \mu \frac{\bar{v}_x}{H} + \rho g_x H. \tag{43}$$

Algebraic manipulation (including the substitution $g_x/g_z = \tan \theta$, where θ is the slope angle) modifies (43) to a canonical form

$$\frac{d\bar{v}_x}{dt} + 3\frac{\nu_f \mu}{\rho H^2}\bar{v}_x = g_z \Theta, \tag{44}$$

in which

$$\Theta = \tan \theta - (1 - \lambda) \tan \varphi_{bed} \tag{45}$$

is a key parameter that represents the normalized gravitational driving force minus resistance due to basal Coulomb friction. Furthermore, Θ is constant if the pore pressure ratio λ, slope angle θ, and friction angle φ_{bed} are constant or if changes in their values cancel one another.

For constant Θ the solution of (44), subject to the initial condition $\bar{v}_x = \bar{v}_0$ at $t = 0$, is

$$\bar{v}_x = \frac{\rho g_z H^2}{3\nu_f \mu}\Theta\left[1 - \exp\left(-t \Big/ \frac{\rho H^2}{3\nu_f \mu}\right)\right] + \bar{v}_0 \exp\left(-t \Big/ \frac{\rho H^2}{3\nu_f \mu}\right). \tag{46}$$

Graphed in Figure 5 for the case $\bar{v}_0 = 0$, (46) is noteworthy in three respects. First, if drag due to lateral boundaries is insignificant compared to basal drag, (46) describes motion of the center of mass of deforming bodies as well as translating bodies. Then, even if Θ varies as an arbitrary function of position or time, (46) can be used as a basis for stepwise calculation of the center-of-mass motion of Coulomb mixtures with either constant or varying λ [cf. *Hutchinson*, 1986]. Second, the motion described by (46) approaches a steady state asymptotically but never becomes fully steady owing to the influence of rate-independent Coulomb resistance. The time necessary to approach steady state can be so long that it is virtually unattainable because the parameter that scales time in (46), $\rho H^2/3\nu_f \mu$, has values $\sim 10^6$ s ($\sim$12 days) for flows 1 m thick in which the fluid is either water or air. Third, a result equivalent to (46) can be obtained by assuming that the mixture obeys a cohesionless, Coulomb viscous rheology like that proposed by *Johnson* [1970]. However, this equivalence arises only in very simple

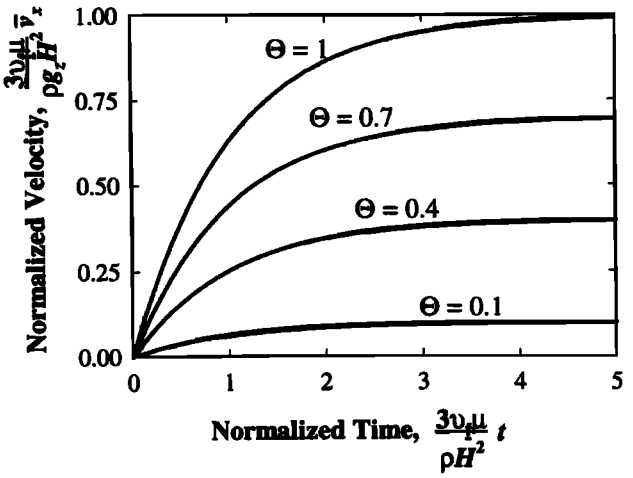

Figure 5. Graphs of unsteady translational motion predicted by equation (46) for typical values of the parameter $\Theta = \tan\theta - (1 - \lambda)\tan\varphi_{bed}$. Steady state velocities are approached only after very long times, indicated by normalized times larger than 1.

problems that involve one-dimensional depth-averaged motion and does not indicate a general correspondence of the Coulomb mixture and Coulomb viscous models.

5.2. Steady Flow in Rectangular Channels

Although steady, uniform flow of a Coulomb mixture is unlikely in nature, as indicated in section 5.1, solutions for this asymptotic limit provide useful insight. In particular, solutions for cross-stream velocity profiles in steady, uniform flows provide a further basis for comparing predictions of the Coulomb mixture model with those of linearly viscoplastic (Bingham), pseudoplastic, and nonlinearly viscoplastic (Herschel-Bulkley) rheological models [cf. *Johnson*, 1970; *Bird et al.*, 1982; *Iverson*, 1985]. Consequently, we consider steady unidirectional flow of a mixture with constant thickness $h = H$ and constant λ (implying a fixed degree of liquefaction) in a rectangular channel inclined at a uniform angle θ in the x direction. In this case the x direction momentum equation (39) reduces to

$$-\rho g_z H(1 - \lambda)\tan\varphi_{bed} - 3\nu_f\mu\frac{\bar{v}_x}{H} + \nu_f\mu H\frac{d^2\bar{v}_x}{dy^2} + \rho g_x H = 0. \tag{47}$$

Algebraic manipulation (including the substitution $g_x/g_z = \tan\theta$) modifies (47) to a canonical form

$$\frac{d^2\bar{v}_x}{d(y/H)^2} - 3\bar{v}_x = \frac{\rho H^2}{\nu_f\mu}g_z\Theta, \tag{48}$$

which has a solution

$$\bar{v}_x = \frac{\rho g_z H^2}{3\nu_f\mu}\Theta\left[1 - \cosh\frac{\sqrt{3}\,y}{H} + \left(\tanh\frac{\sqrt{3}\,Y}{H}\right)\cdot\left(\sinh\frac{\sqrt{3}\,y}{H}\right)\right] \tag{49}$$

that satisfies boundary conditions stipulating zero velocity at the channel margin ($\bar{v}_x = 0$ at $y = 0$) and symmetry of the velocity profile about the channel centerline ($d\bar{v}_x/d(y/H) = 0$ at $y/H = Y/H$). The symmetry boundary dictates that the width-to-depth ratio of the flow is $2Y/H$. The zero-velocity boundary neglects Coulomb slip that may occur at the channel walls because the rate of Coulomb slip is indeterminate in this steady state calculation. Coulomb stresses at channel walls can produce frictional resistance not accounted for in (49), but the neglected friction becomes vanishingly small as the channel width increases ($2Y/H \to \infty$) or as the degree of liquefaction increases ($\lambda \to 1$).

Figure 6 depicts plots of (49) for various values of the parameter $\Theta = \tan\theta - (1 - \lambda)\tan\varphi_{bed}$ and for two different channel configurations, one wide ($2Y/H = 20$) and one narrow ($2Y/H = 2$). The wide channel reflects conditions most common in nature, but the narrow channel helps illustrate the influence of channel constriction. Figure 6a indicates that velocity profiles for wide, channelized flows of grain-fluid mixtures can exhibit narrow marginal shear zones and undeformed medial plugs, similar to those predicted by Bingham, pseudoplastic, and Herschel-Bulkley models and similar to those measured, for example, by *Johnson* [1970, p. 512] and *Pierson* [1986]. However, these undeformed plugs do not indicate the presence of intrinsic yield strength or nonlinear viscous effects. Instead, they reflect trade-offs between lateral shearing and basal drag. Greater degrees of liquefaction (indicated by larger values of λ and Θ) result in decreased basal Coulomb drag,

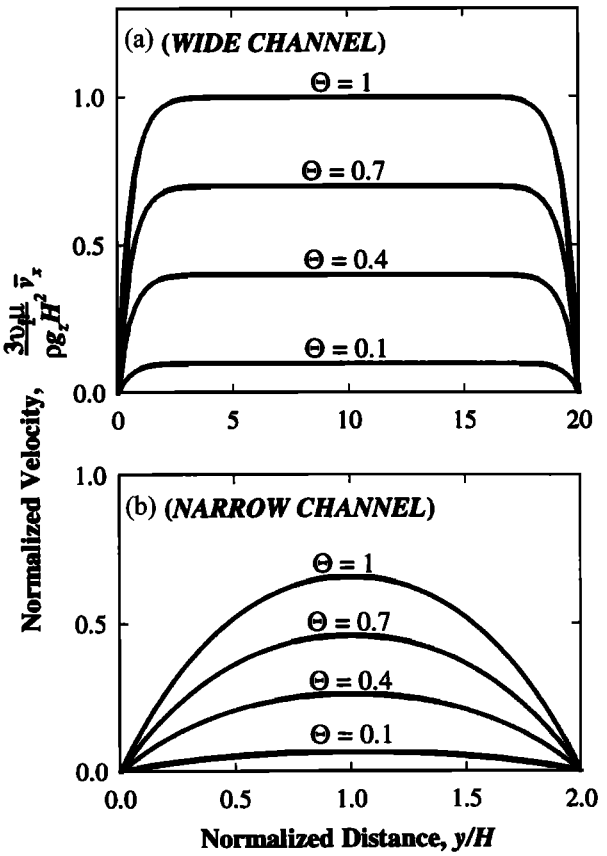

Figure 6. Cross-stream velocity profiles for steady flow in rectangular channels predicted by equation (49) for typical values of the parameter $\Theta = \tan\theta - (1 - \lambda)\tan\varphi_{bed}$. (a) Velocity distribution in a flow with a width-to-depth ratio of 20. (b) Velocity distribution in a flow with a width-to-depth ratio of 2.

increased dominance of viscous drag and lateral shearing, and increased flow velocities.

In comparison to Figure 6a, Figure 6b demonstrates the effect of channel narrowing. As the ratio $2Y/H$ decreases, velocity profiles become rounder, and in the limit $2Y/H \to 0$ they approach the parabolic shape observed in plane Poisuelle flow of a linearly viscous fluid. *Pierson* [1986] measured rounded velocity profiles similar to those in Figure 6b in a debris flow that occurred October 1, 1981, in a narrow canyon on the flank of Mount St. Helens, Washington.

5.3. Static Equilibrium of Source Areas and Deposits

Because our model simulates the behavior of grain-fluid flows from initiation to deposition, the equations can describe static states of limiting equilibrium as well as states of flow. Solutions for static, limit equilibrium profiles of regolith mantles on hillslopes provide a benchmark for comparing our model with well-known slope stability models, and solutions for limit equilibrium profiles of partly liquefied but static deposits provide a basis for comparing our model predictions with features commonly observed in the field. In the static limit ($\bar{v}_x = 0$, $\bar{v}_y = 0$) the x direction momentum equation (39) reduces to

$$(\rho g_z h - p_{bed}) \tan \varphi_{bed} + h k_{act/pass} \frac{\partial}{\partial x} (\rho g_z h - p_{bed}) + h \frac{\partial p_{bed}}{\partial x}$$

$$+ h k_{act/pass} \frac{\partial}{\partial y} (\rho g_z h - p_{bed}) \sin \varphi_{int} = \rho g_x h, \qquad (50)$$

where we have assumed that sgn $(\bar{v}_x)$ and sgn $(\partial \bar{v}_x/\partial y)$ are positive, conditions applicable if incipient motion occurs in the positive x direction and is resisted by boundary shear in a region where $\partial h/\partial y > 0$. Identification of the direction of motion and the sense of shear is necessary to evaluate the sgn functions in (39), even for static states where motion is incipient rather than real.

To simplify (50), we assume that $k_{act/pass} = 1$, which reduces (50) to the applicable limiting forms for most static states. Some algebraic manipulation then yields

$$\left(1 - \frac{p_{bed}}{\rho g_z h}\right) \tan \varphi_{bed} + \frac{\partial h}{\partial x} + \frac{\partial}{\partial y}\left(h - \frac{p_{bed}}{\rho g_z}\right) \sin \varphi_{int} = \frac{g_x}{g_z}. \qquad (51)$$

When used together with an analogous equation for the y direction, (51) provides a basis for a "method of columns" analysis of the static stability of irregularly shaped three-dimensional slopes [cf. *Hungr et al.*, 1989].

Implications of (51) are clearest for the simple case in which incipient motion occurs in a slab of granular debris resting on an infinitely extensive planar slope inclined at an angle θ in the x-z plane. Then y direction derivatives are zero, $g_x/g_z = \tan \theta$, and (51) reduces to

$$\frac{dh}{dx} = \tan \theta - \tan \varphi_{bed}\left(1 - \frac{p_{bed}}{\rho g_z h}\right) = \Theta. \qquad (52)$$

This equation has solutions that are particularly simple if we assume Θ is constant. In such cases, from (52) and (45) we find

$$\frac{h}{H} = \Theta \frac{x}{H} + 1, \qquad (53)$$

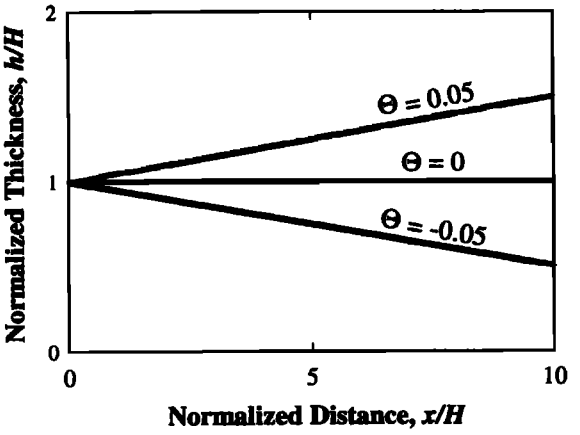

Figure 7. Limiting equilibrium longitudinal profiles of static hillslope debris thickness predicted by equation (53) for typical values of the parameter $\Theta = \tan \theta - (1 - \lambda) \tan \varphi_{bed}$. Values of this parameter appropriate for static equilibrium are apt to be smaller than values appropriate in the dynamic cases illustrated in Figures 5 and 6. A wide variety of nonlinear profiles (described by equation (54)) can satisfy equilibrium if the basal pore pressure distribution is nonuniform.

which obeys a boundary condition stipulating a debris thickness $h = H$ at an arbitrary position $x = 0$.

Values of the parameter Θ control the behavior of (53), as illustrated in Figure 7. For example, $\Theta = 0$ reduces (53) to the standard equation describing limiting equilibrium of a cohesionless infinite slope, commonly used in elementary analyses of slope stability [cf. *Bromhead*, 1986; *Iverson*, 1992]. In this case, $\tan \theta = (1 - \lambda) \tan \varphi_{bed}$ and $h/H = 1$, indicating that a granular mass at limiting equilibrium has a uniform thickness. In cases with $\Theta \neq 0$ a mass of debris resting on a planar substrate will have a nonuniform limit equilibrium thickness, as depicted in Figure 7. If $\Theta \neq 0$ and nonuniform distributions of basal pore fluid pressure exist ($\lambda = \lambda(x)$), additional elementary solutions of (52) predict a wide variety of limit equilibrium hillslope debris thicknesses, described by

$$\frac{h}{H} = (\tan \theta - \tan \varphi_{bed}) \frac{x}{H} + \frac{\tan \varphi_{bed}}{H} \int \lambda(x)\, dx. \qquad (54)$$

Equation (52) can also be used to assess static equilibrium profiles of deposits. For simple cases in which $p_{bed} = 0$ the equation predicts that the surface slope $\tan \theta - dh/dx$ of a static mass of Coulomb material at limiting equilibrium will be a constant, $\tan \varphi_{bed}$ (although no material will remain on the slope if $\theta > \varphi_{bed}$). Thus (52) indicates that the angle of repose of a pile of dry granular material depends only the basal friction angle, whereas angles of repose actually depend on both the basal and internal friction angles. Omission of internal friction in (52) results from depth averaging, but the consequent error is modest because basal and internal friction angles seldom differ by more than several degrees. Also, (52) predicts lower angles of repose if positive pore pressures are present.

Equation (52) predicts nonlinear deposit profiles if p_{bed} varies as a function of the distance from deposit margins, as documented by *Major and Iverson* [1999]. For example, specifying $\lambda = h/H$ (where H is the maximum deposit thickness) as a linear approximation of the pore pressure distribution in

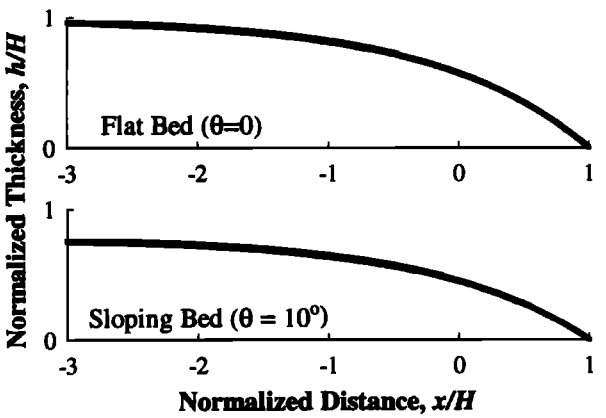

Figure 8. Limit equilibrium longitudinal profiles of static deposits predicted by equation (56) for $\varphi_{bed} = 40°$ and for flat and gently sloping bed surfaces.

freshly emplaced deposits, we obtain a specialized version of (52):

$$\frac{dh}{dx} = \tan\theta - \tan\varphi_{bed}\left(1 - \frac{h}{H}\right), \tag{55}$$

which has a solution

$$\frac{h}{H} = \frac{\tan\theta - \tan\varphi_{bed}}{\tan\varphi_{bed}}\left[\exp\left(\frac{x - x_0}{H}\tan\varphi_{bed}\right) - 1\right] \tag{56}$$

that obeys a boundary condition stipulating the deposit thickness is zero at its margin, located an arbitrary distance $x = x_0$ from the origin (i.e., $h/H = 0$ at $x/H = x_0/H$).

Figure 8 depicts graphs of (56) for cases in which $x_0/H = 1$ and deposits rest on a flat bed ($\theta = 0$) or gently sloping bed ($\theta = 10°$). In each case the surface slope at the deposit margin is $\tan\varphi_{bed}$, and the slope gradually flattens behind the margin to approach $\tan\theta$ asymptotically. These profiles represent type examples rather than predictions for any specific deposit because differing pore pressure distributions and differing values of θ and φ_{bed} will, of course, produce somewhat different profiles. Moreover, emplacement of deposits may be influenced by piecemeal sediment accumulation not represented in (52), (53), or (56) and by accumulation and imbrication of exceptionally large clasts (with diameters comparable to the maximum flow depth) that steepen flow fronts to slopes greater $\tan\varphi_{bed}$. Despite these complications, the profiles shown in Figure 8 have forms that resemble those of many deposits.

6. Scaling, Pore Pressures, and Scale Modeling

Rigorous testing of model predictions requires closely controlled physical experiments in which values of all relevant parameters are known. However, controlled physical experiments typically cannot be conducted at scales like those of important geophysical events. Guidance for design and interpretation of scaled-down physical experiments results from normalization of the governing equations and evaluation of the scaling parameters the normalized equations contain.

In the x momentum equation (39) we define normalized variables as [cf. *Iverson*, 1997b] $x^* = x/L$, $y^* = y/L$, $r_x^* = r_x/L$, $\bar{v}_x^* = \bar{v}_x/\sqrt{gL}$, $\bar{v}_y^* = \bar{v}_y/\sqrt{gL}$, $t^* = t/\sqrt{L/g}$, $h^* = h/H$, $p_{bed}^* = p_{bed}/(\rho g H)$, $g_z^* = g_z/g = \cos\theta_x$, and $g_x^* = g_x/g = \sin\theta_x$. These definitions indicate the importance of two length scales, L and H, first noted by *Savage and Hutter* [1989]. The scale L applies in the directions of flow (x and y), and the scale H applies normal to the direction of flow (z). Nominally, L may be identified as the maximum length of the flowing mass, and H may be identified as the maximum thickness. Substitution of the normalized variables into (39) and division of all terms by $\rho g H$ yields a normalized x momentum equation

$$\begin{aligned}
&\frac{\partial(h^*\bar{v}_x^*)}{\partial t^*} + \frac{\partial(h^*\bar{v}_x^{*2})}{\partial x^*} + \frac{\partial(h^*\bar{v}_x^*\bar{v}_y^*)}{\partial y^*} \\
&\quad = -\mathrm{sgn}\,(\bar{v}_x^*)(h^*\cos\theta_x - p_{bed}^*)\left[1 + \frac{\bar{v}_x^{*2}}{r_x^*\cos\theta_x}\right]\tan\varphi_{bed} \\
&\quad - \frac{1}{\varepsilon}\frac{3}{N_R}\frac{\bar{v}_x^*}{h^*} - \varepsilon h^* k_{act/pass}\frac{\partial}{\partial x^*}(h^*\cos\theta_x - p_{bed}^*) \\
&\quad - \varepsilon h^*\frac{\partial p_{bed}^*}{\partial x^*} + \varepsilon\frac{h^*}{N_R}\frac{\partial^2\bar{v}_x^*}{\partial x^{2*}} - \mathrm{sgn}\left(\frac{\partial\bar{v}_x^*}{\partial y^*}\right)\varepsilon h^* k_{act/pass} \\
&\quad \cdot\frac{\partial}{\partial y^*}(h^*\cos\theta_x - p_{bed}^*)\sin\varphi_{int} + \varepsilon\frac{h^*}{N_R}\frac{\partial^2\bar{v}_x^*}{\partial y^{2*}} \\
&\quad + h^*\sin\theta_x.
\end{aligned} \tag{57}$$

Two dimensionless scaling parameters result from this normalization,

$$\varepsilon = \frac{H}{L} \qquad N_R = \frac{\rho H\sqrt{gL}}{v_f\mu}. \tag{58}$$

The parameter ε is the typical depth-to-length aspect ratio of a flow, a purely geometric factor that indicates no scale dependence. In contrast, N_R serves as a dynamic scaling factor analogous to the Reynolds number in Newtonian fluid mechanics. For geophysical flows in which H commonly exceeds 1 m and L commonly exceeds tens of meters, values $\varepsilon < 0.01$ and $N_R > 10^6$ apply almost universally (Table 1), indicating that the lowest-order approximation of the resisting stresses in (57) commonly includes only the first (basal Coulomb friction) term on the right-hand side. However, the relative importance of basal Coulomb friction and viscous drag depends on the degree of liquefaction (indicated by the value of p_{bed}^*), which in turn depends on spatial and temporal changes in h^*. Unsteady, nonuniform flow can thereby influence even the lowest-order approximation of flow resistance.

Because N_R appears in the denominators of all viscous terms in (57), it indicates that viscous effects will be less important in large flows (i.e., those with large $H\sqrt{gL}$) than in small flows with the same value of $v_f\mu/\rho$ (the effective kinematic viscosity). For flows in which the intergranular fluid is air or water, only miniature flows with very small values of $H\sqrt{gL}$ are likely to exhibit strong viscous effects because effective kinematic viscosities are likely to fall in the range 10^{-4} to 10^{-6} m^2/s. From this narrow range of values one might also infer that flows of dry grains in air would be dynamically similar to comparably sized water-saturated flows of the same grains. This inference contradicts common experience and indicates that an additional scaling factor related to fluid stresses must exist. An assessment of pore pressure evolution identifies this scaling factor, N_p.

6.1. Evaluation of $p_{bed}(x, y, t)$

In our depth-averaged model the basal pore pressure distribution $p_{bed}(x, y, t)$ determines the degree of mixture fluidization and must itself be determined to complete the solutions for $\bar{v}_x$, $\bar{v}_y$, and h. Rigorous determination of the pore pressure distribution would entail solution of the full, three-dimensional mixture theory equations (4) and (5), but here we use a simpler approach that is compatible with our depth-averaged momentum equations (e.g., equation (39) or (57)) and similar to an approach described by *Savage and Vallance* [1998].

Using measurements reported by *Iverson* [1997a] and *Major and Iverson* [1999] as a guide, we infer that basal pore fluid pressures advect passively with flow in the x and y directions and that pore pressures simultaneously diffuse in the z direction owing to time-dependent mixture consolidation. Pore pressures therefore obey an advective diffusion equation

$$\frac{\partial p_{bed}}{\partial t} + \bar{v}_x \frac{\partial p_{bed}}{\partial x} + \bar{v}_y \frac{\partial p_{bed}}{\partial y} = D \left. \frac{\partial^2 p}{\partial z^2} \right|_{bed}, \qquad (59)$$

in which D is the pore pressure diffusivity of the grain-fluid mixture, and the diffusive term involving $\partial^2 p/\partial z^2$ is evaluated at the bed. By employing the same dimensionless variables used to derive (57) we rewrite (59) in a normalized form

$$\frac{\partial p^*_{bed}}{\partial t^*} + \bar{v}^*_x \frac{\partial p^*_{bed}}{\partial x^*} + \bar{v}^*_y \frac{\partial p^*_{bed}}{\partial y^*} = N_p \left. \frac{\partial^2 p^*}{\partial z^{*2}} \right|_{bed}, \qquad (60)$$

where $z^* = z/H$, $p^* = p/(\rho g H)$, and the dimensionless parameter N_p is defined by

$$N_p = \frac{D\sqrt{L/g}}{H^2}. \qquad (61)$$

This parameter represents the timescale for downslope flow $\sqrt{L/g}$ divided by the timescale for pore pressure diffusion normal to the flow direction, H^2/D. We identify N_p as a crucial scaling factor that accompanies those in (58).

Values $N_p \ll 1$ apply in most geophysical flows and indicate that if high pore pressures develop, they generally persist much longer than does downslope grain flow motion (Table 1). Moreover, because N_p decreases quadratically as the flow thickness H increases, large-scale flows preserve high pore pressures much longer than do small-scale flows with the same mixture composition. In flows of a particular size, pore pressures diffuse more rapidly in grain-air mixtures than in comparably sized grain-water mixtures (owing to differing viscosities of air and water, which produce differing diffusivities), and this difference in diffusion speed can greatly affect flow dynamics.

Small values of N_p ($\ll 1$) indicate that pore pressure advection and diffusion operate on different timescales, which justifies decoupling (60) into separate advection and diffusion equations that can be solved sequentially [cf. *Calhoun and LeVeque*, 2000]. To calculate pore pressures, we first compute the dominant, advective component of pore pressure change by assuming $N_p = 0$ and solving (60) together with the conservation equations for $\bar{v}_x$, $\bar{v}_y$, and h. Following numerical calculation of advective changes in p_{bed} at each time step, we then correct the values of p_{bed} for diffusion by solving the linear equation $\partial p/\partial t|_{bed} = D(\partial^2 p/\partial z^2)|_{bed}$ subject to the initial and boundary conditions

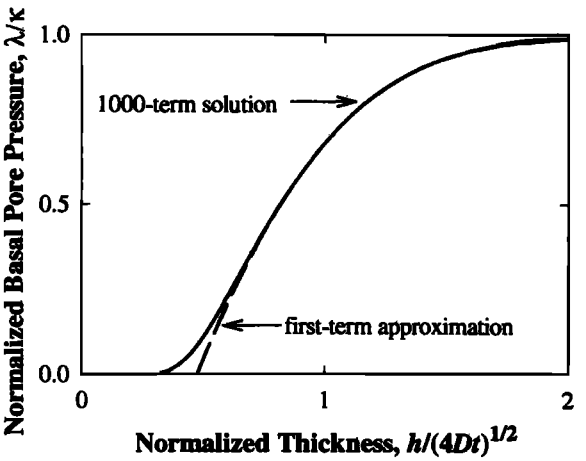

Figure 9. Graph of the normalized basal pore pressure distribution predicted by equation (63). The solid curve represents the first 1000 terms of the series solution. The dashed curve represents the first-term approximation of the series.

$$p(z, 0) = \kappa[\rho g_z(h - z)], \qquad \frac{\partial p}{\partial z}(0, t) = 0, \qquad (62)$$

$$p(h, t) = 0.$$

The initial condition specifies that pore pressures equal a fraction κ ($0 \le \kappa \le 1$) of the total normal stress at every depth z, $\rho g_z(h - z)$. The boundary conditions specify that pore pressure diffusion is directed away from the bed ($z = 0$) and toward the free surface ($z = h$), where the fluid pressure is zero (i.e., background atmospheric pressure). In water-saturated flows the final stages of pore pressure dissipation result from gravitational drainage and ultimately produce pressures less than atmospheric [*Iverson*, 1997a]. In these circumstances, linear pore pressure diffusion is a poor model, but as an approximation, we assume that diffusion proceeds until pressures reach atmospheric values and then ceases.

The solution of the linear diffusion equation, subject to (62), can be obtained easily by adapting a comparable heat conduction solution from *Carslaw and Jaeger* [1959, equation 3.3.9]. The full solution is unnecessary here, however, because our depth-averaged model employs only the pore fluid pressure at the bed, p_{bed}. We evaluate *Carslaw and Jaeger*'s [1959] solution at the bed (where $z = 0$) to obtain

$$\frac{p_{bed}}{\rho g_z h} = \lambda = \kappa\left\{1 - 2\sum_{n=0}^{\infty}\left[(-1)^n \operatorname{erfc}\left((2n+1)\frac{h}{\sqrt{4Dt}}\right)\right]\right\} \qquad (63)$$

in which λ is defined as in (28). Figure 9 depicts graphs of (63) computed from the first 1000 terms of the infinite series and from the first term (i.e., $n = 0$) alone. The curves illustrate that for $h/\sqrt{4Dt} > \sim 0.5$, the series in (63) converges very rapidly and the first-term approximation is quite good. For $h/\sqrt{4Dt} < \sim 0.5$, the first-term approximation is poor, but $\lambda = 0$ is a good alternative approximation. We use these approximations in our numerical solutions [*Denlinger and Iverson*, this issue].

Figure 9 has a simple but important physical interpretation if it is viewed as a snapshot of the basal pore pressure distribution at a fixed time t in a steady flow of variable thickness h.

Near flow margins, where sediment thicknesses are sufficiently small, pore pressures are essentially zero ($\lambda \rightarrow 0$) and Coulomb friction is consequently high. In contrast, Coulomb friction is low where sediment thicknesses are sufficiently thick that high pore pressures are maintained. Of course, pore pressure dissipation occurs fastest where hydraulic diffusivities are largest. For example, if $D = 10^{-4}$ m^2/s (a relatively large value typical of debris flow mixtures containing only sand- and gravel-sized sediment; Table 1) and $h = 1$ m, Figure 9 indicates that basal pore pressures will decay to about half their original magnitude in ~1 min.

6.2. Implications for Scale-Model Experiments

Increasing values of the scaling parameters N_R and N_p indicate increasing dominance of Coulomb stresses and decreasing importance of fluid stresses. However, if flow size increases while solid and fluid properties remain fixed, N_p decreases, while N_R increases. The disparate influence of flow size on N_R and N_p can pose a severe problem in scale model experiments. For example, miniature flows of grain-water mixtures cannot emulate conditions in full-scale geophysical flows, where small values of N_p indicate that effects of persistent high fluid pressure may be very significant, but large values of N_R indicate that shear stresses due to fluid viscosity may be negligible. Decrease of N_p with increasing flow size also indicates that persistent basal fluid pressures may enhance the mobility of the largest flows the most [cf. *Shreve*, 1968].

Electrostatic phenomena that operate at molecular scales also can bedevil miniature experiments. Electrostatic forces produce macroscopic adhesive forces such as intergranular cohesion and surface tension at fluid interfaces. Such forces are fundamentally scale-independent and therefore have the greatest influence on the smallest grains and smallest flows. For example, a cohesive yield strength ~100 Pa (typical of dense clay slurries [*O'Brien and Julien*, 1988; *Major and Pierson*, 1992]) can balance the total shear stress at the base of a miniature flow 5 mm thick on a 30° slope, but it balances only about one thousandth of the basal shear stress in a flow 5 m thick on the same slope. Thus miniature experiments with clay slurries [e.g., *Coussot and Proust*, 1996] may bear little dynamic similarity to large-scale geophysical flows.

7. Discussion

The Coulomb mixture model can simulate a wide spectrum of grain-fluid flows from initiation to deposition, with no redefinition of parameters. However, parameter values are constrained to differing degrees in different types of flows. In granular avalanches where large values of both N_R and N_p indicate that fluid effects are negligible, model input consists only of initial geometry, flow path topography, and specified values of φ_{int} and φ_{bed}, which are readily estimated and rarely vary outside the range 25°–45°. In such cases the model requires virtually no calibration.

For cases in which fluid stresses play a significant role, additional model input consists of mixture bulk density ρ, which rarely varies outside the range 1000–2200 kg/m^3; pore fluid viscosity μ, which varies quite predictably depending on whether the fluid is dominantly air, water, or "dirty" air or water containing suspended fine sediment [*Iverson*, 1997a]; initial conditions for pore fluid pressure, specified by $0 \leq \kappa \leq 1$; and a diffusivity D that governs dissipation of pore fluid pressure (Table 1). Of these parameters, D probably varies the most among flows and from place to place in individual flows. Values of D depend on the pore fluid viscosity μ but also on the aggregate permeability k and stiffness, each of which can vary by many orders of magnitude as a function of the grain size distribution, porosity, and degree of mixture agitation [*Iverson*, 1997a]. For debris flow mixtures composed predominantly of sand and gravel, measured diffusivities fall in the range 10^{-3}–10^{-7} m^2/s [*Iverson*, 1997a; *Major et al.*, 1997], but diffusivities larger than 10^{-3} m^2/s may exist in debris flow snouts, where grain size segregation commonly produces a concentration of gravel, cobbles, and boulders [*Suwa*, 1988]. Diffusivities of rock avalanches are probably similar to those in debris flow snouts, whereas diffusivities of fine-grained pyroclastic flows are probably smaller, as evidenced by the longevity of fluidization in deposit interiors [*Wilson and Head*, 1981]. Of course, the concept of diffusivity itself loses validity if pore fluid flow relative to adjacent solid grains becomes sufficiently rapid that piping and bubbling occur. Further investigation of pore pressure diffusivities in diverse grain-fluid mixtures with varying degrees of agitation is clearly warranted.

Even if flows are quite rapid and highly agitated, the depth-averaged Coulomb mixture model might provide an acceptable description of bulk flow dynamics. The depth-averaged model uses the Coulomb rule to predict a ratio of shear to normal stresses that is nearly identical to that predicted by the *Bagnold* [1954] grain collision model. Moreover, basal normal stresses must balance the weight of the overlying material in all depth-averaged models. Therefore basal shear stresses predicted by depth-averaged Coulomb and Bagnold models are nearly identical, and basal shear stresses constitute the lowest-order approximation of total flow resistance, as shown in equation (57). The salient difference between the Coulomb and Bagnold models entails only *Bagnold*'s [1954] coupling of shear and normal stresses to shear rate and solid volume fraction. If solid volume fractions differ little from static values (ranging from 0.5 to 0.7, for example, in most debris flows [*Iverson*, 1997a]) and the surface elevations of flows adjust freely to accommodate dilation and balance the ambient stresses, the effect of *Bagnold*'s [1954] coupling on depth-averaged behavior may be minimal.

The predictive power of the Coulomb mixture model is illustrated best by numerical calculations of unsteady, multidimensional flows, treated by *Denlinger and Iverson* [this issue]. Such calculations highlight the importance of flow path topography by demonstrating that total resistance commonly depends more on boundary geometry (i.e., "form drag") than on boundary shear stresses (i.e., "skin friction").

Perhaps the greatest limitation on the model's predictive capability results from the assumption that flows maintain constant masses as they move downslope. Mass change is an important feature of some debris flows and avalanches, and although mass change terms may be appended to the model equations with little difficulty, the magnitude of such terms depends on external forces which are poorly constrained in most instances.

8. Conclusions

The Coulomb mixture model has several features not shared by previous models of geophysical grain-fluid flows. Foremost, it accounts explicitly for stresses and interactions of distinct solid and fluid constituents and eliminates the need to specify rheologies of complex, multiphase mixtures. Instead, the effec-

tive mixture rheology evolves as a consequence of simple interactions between solid-phase Coulomb friction and fluid-phase viscosity and pressure. The model also includes other important features not present in competing models, such as mathematical frame invariance and transverse shear stresses than act on surfaces normal to flow directions. These features appear crucial for analyzing flow interaction with three-dimensional terrain.

Coulomb mixture theory blurs time-honored distinctions between phenomena such as landslides, debris avalanches, debris flows, and slurry floods. Viewed in the Coulomb mixture context, one type of phenomenon grades smoothly into another as a result of changes in fluid content and mixture fluidization. Classification schemes that distinguish mass movement phenomena primarily on the basis of provenance or appearance [e.g., *Cruden and Varnes*, 1996] serve a utilitarian need for communication but provide less understanding than that gained by assessing the distinctive roles of solid and fluid forces.

Although many implications of the depth-averaged Coulomb mixture equations are revealed only by numerical solutions for unsteady, multidimensional flows [*Denlinger and Iverson*, this issue], exact analytical solutions of simplified equations provide important insight. For example, analytical solutions demonstrate that steady flow of Coulomb mixtures is implausible in nature, owing to the long time required to attain steady states. Solutions for the asymptotic limit of steady flow in rectangular channels demonstrate that Coulomb mixtures may develop undeformed medial plugs bounded by marginal shear zones. In other cases, such undeformed plugs may be absent, and in no case does plug formation constrain mixture rheology or imply the existence of intrinsic yield strength. Solutions for the limiting static forms of hillslopes in mechanical equilibrium demonstrate the connection between the Coulomb mixture equations and equations commonly used in slope stability analyses. Solutions for the static forms of deposits demonstrate that bluntly tapered deposit margins with relatively high frictional strength can contain more fluidized debris in deposit interiors. Deposit thickness reveals little about bulk flow rheology but gives some indication of the constraining influence of large marginal clasts and the extent of mixture fluidization when deposition occurred.

Normalization of the depth-averaged Coulomb mixture equations yields dimensionless scaling parameters that aid design and interpretation of experiments aimed at simulating geophysical flows. As flow size increases, values of the scaling parameter N_R increase and indicate that viscous stresses diminish in importance, whereas values of the scaling parameter N_p decrease and indicate that fluid pressure effects grow more pronounced. This opposing change indicates that insurmountable difficulties may plague miniature experiments that aim to mimic the behavior of geophysical flows in which fluid effects are significant. On the other hand, if fluid effects are negligible, the mixture model reduces to a simpler two-parameter model in which φ_{int}, φ_{bed}, initial conditions, and path geometry control flow dynamics completely. Such flows represent a limiting case that may be scaled down relatively easily.

Acknowledgments. We thank Joseph Walder, Jeff Johnson, David McClung, Gary Parker, and an anonymous reviewer for thoughtful critiques of the manuscript.

References

Abramowitz, M., and I. A. Stegun (Eds.), *Handbook of Mathematical Functions with Formulas, Graphs, and Mathematical Tables*, U.S. Dept. of Commer., Natl. Inst. of Stand. and Technol., Gaithersburg, Md., 1964.

Adams, M. J., and B. J. Briscoe, Deterministic micromechanical modeling of failure or flow in discrete planes of densely packed particle assemblies: Introductory principles, in *Granular Matter*, edited by A. Mehta, pp. 259–291, Springer-Verlag, New York, 1994.

Atkin, R. J., and R. E. Craine, Continuum theories of mixtures: Basic theory and historical development, *Q. J. Mech. Appl. Math.*, *29*(2), 209–244, 1976.

Bagnold, R. A., Experiments on a gravity-free dispersion of large solid spheres in a Newtonian fluid under shear, *Proc. R. Soc. London, Ser. A*, *225*, 49–63, 1954.

Bear, J., *Dynamics of Fluids in Porous Media*, 764 pp., Dover, Mineola, N. Y., 1972.

Bird, R. B., W. E. Stewart, and E. N. Lightfoot, *Transport Phenomena*, 780 pp., John Wiley, New York, 1960.

Bird, R. B., G. C. Dai, and B. J. Yaruso, The rheology and flow of viscoplastic materials, *Rev. Chem. Eng.*, *1*, 1–70, 1982.

Bromhead, E. N., *The Stability of Slopes*, 374 pp., Chapman and Hall, New York, 1986.

Brown, R. L., and J. C. Richards, *Principles of Powder Mechanics*, 221 pp., Pergamon, Tarrytown, N. Y., 1970.

Calhoun, D., and R. J. LeVeque, A Cartesian grid finite-volume method for the advection-diffusion equation in irregular geometries, *J. Comput. Phys.*, *157*, 143–180, 2000.

Carslaw, H. S., and J. C. Jaeger, *Conduction of Heat in Solids*, 2nd ed., 510 pp., Oxford Univ. Press, New York, 1959.

Coulomb, C. A., Sur une application des régles de maximis &minimis à quelques problèms de statique, reltifs à l'architecture, in *Mémoires de Mathématique et de Physique, Presented at the Royal Academy of Sciences, 1773*, pp. 343–384, Imp. R. Acad. Sci., Paris, 1776.

Coussot, P., and S. Proust, Slow unconfined spreading of a mudflow, *J. Geophys. Res.*, *101*(B11), 25,217–25,229, 1996.

Cruden, D. M., and D. J. Varnes, Landslide types and processes, in *Landslides Investigation and Mitigation*, edited by A. K. Turner and R. L. Schuster, pp. 36–75, Natl. Acad. Press, Washington, D. C., 1996.

Denlinger, R. P., and R. M. Iverson, Flow of variably fluidized granular masses across three-dimensional terrain, 2, Numerical predictions and experimental tests, *J. Geophys. Res.*, this issue.

Desai, C. S., and H. J. Siriwardane, *Constitutive Laws for Engineering Materials, With Emphasis on Geologic Materials*, 468 pp., Prentice-Hall, Englewood Cliffs, N. J., 1984.

Duran, J., *Sands, Powders, and Grains—An Introduction to the Physics of Granular Materials*, 214 pp., Springer, New York, 2000.

Gidaspow, D., *Multiphase Flow and Fluidization*, 467 pp., Academic, San Diego, Calif., 1994.

Gray, J. M. N. T., M. Wieland, and K. Hutter, Gravity driven free surface flow of granular avalanches over complex basal topography, *Proc. R. Soc. London, Ser. A*, *455*, 1841–1874, 1999.

Hoblitt, R. P., Observations of the eruptions of July 22 and August 7, 1980, at Mount St. Helens, Washington, *U.S. Geol. Surv. Prof. Pap.*, *1335*, 44 pp., 1986.

Hsu, K. J., Catastrophic debris streams (sturzstroms) generated by rockfalls, *Geol. Soc. Am. Bull.*, *86*, 129–140, 1975.

Hsu, K. J., Albert Heim: Observations on landslides and relevance to modern interpretations, in *Rockslides and Avalanches*, vol. 1, *Natural Phenomena*, edited by B. Voight, pp. 71–93, Elsevier Sci., New York, 1978.

Hubbert, M. K., and W. W. Rubey, Role of fluid pressures in mechanics of overthrust faulting, I, Mechanics of fluid-filled porous solids and its applications to overthrust faulting, *Geol. Soc. Am. Bull.*, *70*, 115–166, 1959.

Hungr, O., F. M. Salgado, and P. M. Byrne, Evaluation of a three-dimensional method of slope stability analysis, *Can. Geotech. J.*, *26*, 679–686, 1989.

Hutchinson, J. N., A sliding-consolidation model for flow slides, *Can. Geotech. J.*, *23*, 115–126, 1986.

Iverson, R. M., A constitutive equation for mass-movement behavior, *J. Geol.*, *93*, 143–160, 1985.

Iverson, R. M., Sensitivity of stability analyses to groundwater data, in *Landslides (Proceedings of the Sixth International Symposium on*

Landslides, 1), edited by D. H. Bell, pp. 451–457, A. A. Balkema, Brookfield, Vt., 1992.

Iverson, R. M., Differential equations governing slip-induced pore-pressure fluctuations in a water-saturated granular medium, *Math. Geol., 23*, 1027–1048, 1993.

Iverson, R. M., The physics of debris flows, *Rev. Geophys., 35*, 245–296, 1997a.

Iverson, R. M., Hydraulic modeling of unsteady debris-flow surges with solid-fluid interactions, in *Debris-Flow Hazards Mitigation: Mechanics Prediction and Assessment*, edited by C. L. Chen, pp. 550–560, Am. Soc. Civ. Eng., Reston, Va., 1997b.

Iverson, R. M., and R. G. LaHusen, Dynamic pore-pressure fluctuations in rapidly shearing granular materials, *Science, 246*, 769–799, 1989.

Iverson, R. M., M. E. Reid, and R. G. LaHusen, Debris-flow mobilization from landslides, *Ann. Rev. Earth Planet. Sci., 25*, 85–138, 1997.

Johnson, A. M., *Physical Processes in Geology*, 577 pp., W. H. Freeman, New York, 1970.

Lambe, T. W., and R. V. Whitman, *Soil Mechanics, SI Version*, 553 pp., John Wiley, New York, 1979.

Major, J. J., and R. M. Iverson, Debris-flow deposition—Effects of pore-fluid pressure and friction concentrated at flow margins, *Geol. Soc. Am. Bull., 111*, 1424–1434, 1999.

Major, J. J., and T. C. Pierson, Debris flow rheology: Experimental analysis of fine-grained slurries, *Water Resour. Res., 28*, 841–857, 1992.

Major, J. J., R. M. Iverson, D. F. McTigue, S. Macias, and B. K. Fiedorowicz, Geotechnical properties of debris-flow sediments and slurries, in *Debris-Flow Hazards Mitigation: Mechanics Prediction and Assessment*, edited by C. L. Chen, pp. 249–259, Am. Soc. Civ. Eng., Reston, Va., 1997.

O'Brien, J. S., and P. Y. Julien, Laboratory analysis of mudflow properties, *J. Hydraul. Eng., 114*, 877–887, 1988.

Passman, S. L., and D. F. McTigue, A new approach to the effective stress principle, in *Compressibility Phenomena in Subsidence*, edited by S. K. Saxena, pp. 79–91, Eng. Found., New York, 1986.

Pierson, T. C., Flow behavior of channelized debris flows, Mount St. Helens, Washington, in *Hillslope Processes*, edited by A. D. Abrahams, pp. 269–296, Allen and Unwin, Winchester, Mass., 1986.

Rankine, W. J. M., On the stability of loose earth, *Philos. Trans. R. Soc. London, 147*, 9–27, 1857.

Reid, M. E., and R. M. Iverson, Gravity-driven groundwater flow and slope failure potential, 2, Effects of slope morphology, material properties, and hydraulic heterogeneity, *Water Resour. Res., 28*, 939–950, 1992.

Reid, M. E., R. G. LaHusen, and R. M. Iverson, Debris-flow initiation experiments using diverse hydrologic triggers, in *Debris-Flow Hazards Mitigation: Mechanics Prediction and Assessment*, edited by C. L. Chen, pp. 1–11, Am. Soc. Civ. Eng., Reston, Va., 1997.

Rowley, P. D., M. A. Kuntz, and N. S. Macleod, Pyroclastic flow deposits, in *The 1980 Eruptions of Mount St. Helens, Washington*, edited by P. W. Lipman, and D. R. Mullineaux, *U.S. Geol. Surv. Prof. Pap., 1250*, 489–512, 1981.

Savage, S. B., The mechanics of rapid granular flows, *Adv. Appl. Mech., 24*, 289–366, 1984.

Savage, S. B., and K. Hutter, The motion of a finite mass of granular material down a rough incline, *J. Fluid Mech., 199*, 177–215, 1989.

Savage, S. B., and K. Hutter, The dynamics of avalanches of granular materials from initiation to runout, part I, Analysis, *Acta Mech., 86*, 201–223, 1991.

Savage, S. B., and M. Sayed, Stresses developed in dry cohesionless granular materials sheared in an annular shear cell, *J. Fluid Mech., 142*, 391–430, 1984.

Savage, S. B., and J. W. Vallance, Modeling effects of consolidation in unsteady debris-flow surges, *Eos Trans. AGU, 79*(17), Spring Meet. Suppl., S332, 1998.

Schlichting, H., *Boundary-Layer Theory*, 7th ed., 814 pp., McGraw-Hill, New York, 1979.

Shreve, R. L., Leakage and fluidization in air-layer lubricated avalanches, *Geol. Soc. Am. Bull., 79*, 653–658, 1968.

Skempton, A. W., Residual strength of clays in landslides, folded strata and the laboratory, *Geotechnique, 35*, 3–18, 1985.

Suwa, H., Focusing mechanism of large boulders to a debris-flow front, *Trans. Jpn. Geomorphol. Union, 9*, 151–178, 1988.

Takahashi, T., *Debris Flow*, 165 pp., A. A. Balkema, Brookfield, Vt., 1991.

Terzaghi, K., The shearing resistance of saturated soils and the angle between the planes of shear, *Proc. Int. Conf. Soil Mech., 1st*, 54–56, 1936.

Vreugdenhil, C. B., *Numerical Methods for Shallow-Water Flow*, Kluwer Acad., Norwell, Mass., 261 pp., 1994.

Wilson, L., and J. W. Head, Morphology and rheology of pyroclastic flows and their deposits, and guidelines for future observations, in *The 1980 Eruptions of Mount St. Helens, Washington*, edited by P. W. Lipman and D. R. Mullineaux, *U.S. Geol. Surv. Prof. Pap., 1250*, 513–524, 1981.

R. P. Denlinger and R. M. Iverson, U.S. Geological Survey, 5400 MacArthur Blvd., Vancouver, WA 98661. (roger@usgs.gov; riverson@usgs.gov)

(Received January 18, 2000; revised August 11, 2000; accepted August 23, 2000.)